
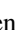

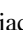
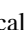




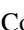

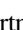






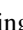



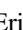
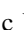









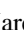







Vetting of 384 TESS Objects of Interest with TRICERATOPS and Statistical Validation of 12 Planet Candidates

Steven Giacalone¹ , Courtney D. Dressing¹ , Eric L. N. Jensen² , Karen A. Collins³ , George R. Ricker⁴ , Roland Vanderspek⁴ , S. Seager^{4,5,6} , Joshua N. Winn⁷ , Jon M. Jenkins⁸ , Thomas Barclay^{9,10} , Khalid Barkaoui^{11,12} , Charles Cadieux¹³ , David Charbonneau³ , Kevin I. Collins¹⁴ , Dennis M. Conti¹⁵ , René Doyon¹³ , Phil Evans¹⁶ , Mourad Ghachoui¹² , Michaël Gillon¹¹ , Natalia M. Guerrero⁴ , Rhodes Hart¹⁷ , Emmanuël Jehin¹⁸ , John F. Kielkopf¹⁹ , Brian McLean²⁰ , Felipe Murgas^{21,22} , Enric Palle^{23,24} , Hannu Parviainen^{23,24} , Francisco J. Pozuelos^{11,25} , Howard M. Relles³ , Avi Shporer⁴ , Quentin Socia^{26,31} , Chris Stockdale²⁷ , Thiam-Guan Tan²⁸ , Guillermo Torres³ , Joseph D. Twicken^{8,29} , William C. Waalkes³⁰ , and Ian A. Waite¹⁷ 

¹ Department of Astronomy, University of California, Berkeley, CA 94720-3411, USA; steven_giacalone@berkeley.edu

² Dept. of Physics & Astronomy, Swarthmore College, Swarthmore, PA 19081, USA

³ Center for Astrophysics | Harvard & Smithsonian, 60 Garden Street, Cambridge, MA 02138, USA

⁴ Department of Physics and Kavli Institute for Astrophysics and Space Research, Massachusetts Institute of Technology, Cambridge, MA 02139, USA

⁵ Department of Earth, Atmospheric and Planetary Sciences, Massachusetts Institute of Technology, Cambridge, MA 02139, USA

⁶ Department of Aeronautics and Astronautics, MIT, 77 Massachusetts Avenue, Cambridge, MA 02139, USA

⁷ Department of Astrophysical Sciences, Princeton University, Princeton, NJ 08544, USA

⁸ NASA Ames Research Center, Moffett Field, CA 94035, USA

⁹ NASA Goddard Space Flight Center, 8800 Greenbelt Road, Greenbelt, MD 20771, USA

¹⁰ University of Maryland, Baltimore County, 1000 Hilltop Circle, Baltimore, MD 21250, USA

¹¹ Astrobiology Research Unit, Université de Liège, 19C Allée du 6 Août, B-4000 Liège, Belgium

¹² Oukaimeden Observatory, High Energy Physics and Astrophysics Laboratory, Cadi Ayyad University, Marrakech, Morocco

¹³ Institute for Research on Exoplanets (iREx), Université de Montréal, Département de Physique, C.P. 6128 Succ. Centre-ville, Montréal, QC H3C 3J7, Canada

¹⁴ George Mason University, 4400 University Drive, Fairfax, VA 22030 USA

¹⁵ American Association of Variable Star Observers, 49 Bay State Road, Cambridge, MA 02138, USA

¹⁶ El Sauce Observatory, Coquimbo Province, Chile

¹⁷ Centre for Astrophysics, University of Southern Queensland, Toowoomba, QLD, 4350, Australia

¹⁸ Space Sciences, Technologies and Astrophysics Research (STAR) Institute, Université de Liège, Allée du 6 août 19C, B-4000 Liège, Belgium

¹⁹ Department of Physics and Astronomy, University of Louisville, Louisville, KY 40292, USA

²⁰ Space Telescope Science Institute, 3700 San Martin Drive, Baltimore, MD 21218, USA

²¹ Instituto de Astrofísica de Canarias (IAC), E-38205 La Laguna, Tenerife, Spain

²² Departamento de Astrofísica, Universidad de La Laguna (ULL), E-38206 La Laguna, Tenerife, Spain

²³ Instituto de Astrofísica de Canarias (IAC), 38205 La Laguna, Tenerife, Spain

²⁴ Departamento de Astrofísica, Universidad de La Laguna (ULL), E-38206, La Laguna, Tenerife, Spain

²⁵ Space Sciences, Technologies and Astrophysics Research (STAR) Institute, Université de Liège, 19C Allée du 6 Août, B-4000 Liège, Belgium

²⁶ Department of Astronomy/Steward Observatory, The University of Arizona, 933 N. Cherry Avenue, Tucson, AZ 85721, USA

²⁷ Hazelwood Observatory, Australia

²⁸ Perth Exoplanet Survey Telescope, Perth, Western Australia

²⁹ SETI Institute, Mountain View, CA 94043, USA

³⁰ Department of Astrophysical and Planetary Sciences, University of Colorado, Boulder, CO 80309, USA

Received 2020 January 30; revised 2020 October 23; accepted 2020 October 30; published 2020 December 11

Abstract

We present TRICERATOPS, a new Bayesian tool that can be used to vet and validate TESS Objects of Interest (TOIs). We test the tool on 68 TOIs that have been previously confirmed as planets or rejected as astrophysical false positives. By looking in the false-positive probability (FPP)—nearby false-positive probability (NFPP) plane, we define criteria that TOIs must meet to be classified as validated planets ($FPP < 0.015$ and $NFPP < 10^{-3}$), likely planets ($FPP < 0.5$ and $NFPP < 10^{-3}$), and likely nearby false positives ($NFPP > 10^{-1}$). We apply this procedure on 384 unclassified TOIs and statistically validate 12, classify 125 as likely planets, and classify 52 as likely nearby false positives. Of the 12 statistically validated planets, 9 are newly validated. TRICERATOPS is currently the only TESS vetting and validation tool that models transits from nearby contaminant stars in addition to the target star. We therefore encourage use of this tool to prioritize follow-up observations that confirm bona fide planets and identify false positives originating from nearby stars.

Unified Astronomy Thesaurus concepts: [Exoplanet astronomy \(486\)](#); [Astrostatistics \(1882\)](#); [Planet hosting stars \(1242\)](#); [Exoplanets \(498\)](#)

Supporting material: machine-readable table

1. Introduction

Over the past decade, the Kepler space telescope has revolutionized our understanding of exoplanets by facilitating

the discovery of thousands of planets that transit in front of their host stars. Among other things, these planets have been useful for investigating the frequency of planets as a function of size and orbital period (e.g., Howard et al. 2012; Dong & Zhu 2013; Dressing & Charbonneau 2013; Fressin et al. 2013; Petigura et al. 2013; Foreman-Mackey et al. 2014;

³¹ Earths in Other Solar Systems Team.

Morton & Swift 2014; Sanchis-Ojeda et al. 2014; Burke et al. 2015; Dressing & Charbonneau 2015; Mulders et al. 2015a, 2015b; Fulton et al. 2017; Hsu et al. 2018), as well as testing theories of planet formation and evolution (e.g., Lopez & Fortney 2013; Swift et al. 2013; Königl et al. 2017; Lee & Chiang 2017; Giacalone et al. 2017). To ensure the veracity of their results, studies that utilized the Kepler data set required (1) that the measured radii of these planets were accurate and (2) that the discovered objects were actually planets. However, due to the limited $4'' \text{ pixel}^{-1}$ resolution of the camera used by Kepler, these two requirements could not always be assumed true. Because it was not uncommon for Kepler field stars of comparable brightness to reside $<4''$ apart, the presence of multiple unresolved stars within a given set of pixels could not be discounted. This uncertainty was problematic because the existence of unresolved stars could cause an underestimation of the radius of a transiting object, sometimes to the extent that an eclipsing binary star could be mistaken for a transiting planet with a fraction of the size.

A number of methods have been used to constrain the possibility of an unresolved star residing within a given pixel. One method used is to search for offsets in the centroid of the source during transit, a signal indicative of another star residing elsewhere in the pixel (e.g., Bryson et al. 2013; Coughlin et al. 2014). Multiband time-series photometry has also been used to search for unresolved stars, as one would expect a different transit depth in different photometric bands if the transiting object is around a star of a different color than the target (e.g., Alonso et al. 2004). Spectra of the target star can also be useful in this vetting process. High-precision radial velocities can rule out bound stellar companions by measuring the masses of transiting objects and monitoring for longer-period secondaries (e.g., Ermann et al. 2014), and reconnaissance spectroscopy can rule out bright unresolved stars by searching for additional lines in the spectrum of the target star (e.g., Santerne et al. 2012; Kolbl et al. 2014). Finally, high-resolution imaging can rule out unresolved stars beyond a fraction of an arcsecond from the target star (e.g., Crossfield et al. 2016; Mayo et al. 2018). Unfortunately, these techniques do not cover the full allowed parameter space individually, and Kepler planet candidate hosts were often too faint for precise radial velocity measurements. For this reason, it was common to turn to vetting and statistical validation to assess the genuineness of Kepler planet candidates.

When speaking of vetting, we refer to the process of scrutinizing the photometry of threshold-crossing events (TCEs, periodic transit-like signals originating from target stars) and classifying them as planet candidates and false positives of instrumental or astrophysical origin. Vetting procedures typically make use of automated decision-making algorithms to determine the natures of these events. Autovetter (McCauliff et al. 2015; Catanzarite 2015) and Robovetter (Thompson et al. 2018) are Kepler-era vetting procedures that classify TCEs based on Kepler data using random forest and decision tree algorithms. DAVE (Kostov et al. 2019) is a vetting tool that calculates metrics based on centroid position and transit shape to classify *K2* and *TESS* TCEs. Lastly, Exonet (Shallue & Vanderburg 2018) and Astronet (Ansdell et al. 2018) make use of convolutional neural networks to classify TCEs based on transit shape. By distinguishing planet candidates from false positives, these tools have allowed

others to focus planetary confirmation and characterization efforts on the most promising targets.

When speaking of statistical validation, we refer to the process of statistically ruling out astrophysical false-positive scenarios to a degree of certainty high enough to advance the status of a planet candidate to one similar to that of a planet confirmed via mass measurement. In addition to information gleaned from the light curve of a planet candidate, validation algorithms typically incorporate constraints obtained from follow-up observations like those described previously. A number of statistical validation algorithms were used during the Kepler era in order to grow the data set with which large-scale studies of planetary system properties could be conducted.

The first Kepler-era validation framework was BLENDER (Torres et al. 2004, 2005, 2010b). BLENDER begins by generating synthetic light curves using models of transiting planets and astrophysical false positives involving blended eclipsing binaries. Next, it calculates the χ^2 of the best-fit planetary scenario and the χ^2 values for several false-positive scenarios over a grid of model parameters. For each false-positive scenario, the region of parameter space where the scenario is viable (defined by where χ^2 differs from the best-fit planetary χ^2 with a confidence level $<3\sigma$) is identified. The properties of the blended stars in these viable instances are then compared to constraints obtained from supplementary follow-up, such as high-resolution imaging and spectroscopy, to determine whether they are physically possible. In addition to this light-curve analysis, BLENDER calculates the multicolor photometry one would expect to measure for each false-positive scenario to compare to the actual observed colors. If the properties of all viable false-positive scenarios are ruled out by the information from these external observations, the planet candidate is considered validated.

BLENDER offered a robust option for the statistical validation of transiting planet candidates during the Kepler era. However, the hands-on nature of the algorithm and the long computation times required to simulate the many false-positive scenarios involved in its analysis made it inefficient for validating planet candidates in bulk. This led to the formulation of a different validation procedure by the name of VESPA (Morton 2012, 2015). In addition to being fully automated, VESPA provides a more computationally expedient option for validating planet candidates by replacing the physical transit models employed in BLENDER with a simpler trapezoidal model, which can capture the most important features of the transit shape with fewer free parameters.

VESPA works in a Bayesian framework where the probabilities of several transit-producing scenarios are computed. For every scenario, VESPA uses the TRILEGAL galactic model (Girardi et al. 2005) to simulate a population of stars with properties consistent with the target star in a cone around the line of sight to the target. The properties of these simulated stars are inferred using archival photometry of the target star and isochrone interpolation, which ensures agreement with observational constraints. For each instance of each population, the transit shape is characterized using a trapezoidal model, which allows for the generation of a trapezoidal parameter prior distribution for each scenario. VESPA then uses a Markov Chain Monte Carlo routine to fit the Kepler light curve to the same trapezoidal model to determine the region of parameter space the target occupies. Next, the marginal likelihood is calculated for every scenario by integrating the

product of the trapezoidal likelihood and parameter prior over the predetermined region of parameter space. These marginal likelihoods are multiplied by model priors based on the geometries of simulated systems and assumptions relating to the occurrence of planets and close binaries. Lastly, the probability of the transiting planet scenario is assessed by comparing this product for the transiting planet scenario with those of all false-positive scenarios, with the planet candidate being validated if the overall false-positive probability (FPP) is $<1\%$. Like BLENDER, VESPA can also incorporate follow-up observations to obtain tighter constraints on this probability.

Another procedure used to validate exoplanet candidates is PASTIS (Díaz et al. 2014; Santerne et al. 2015). PASTIS provides a rigorous option for the statistical validation of small planetary transits by calculating the Bayesian odds ratio between the transiting planet scenario and all possible false-positive scenarios for a given target star. Prior probabilities are computed for each scenario by combining information about the target, including that contained within ground-based follow-up observations, with knowledge of stellar multiplicity and planet occurrence rates. In addition, for false-positive scenarios that involve an unresolved foreground or background star, TRILEGAL is used to simulate a population of stars around the line of sight to target to calculate the prior probability of such a chance alignment. Like in VESPA, these priors are combined with marginal likelihoods, which PASTIS calculates using importance sampling. However, unlike VESPA, PASTIS additionally models the radial velocities of its targets and uses physical light-curve models in its analysis. Like those utilized with BLENDER, these light-curve models are more complex than the trapezoidal model, meaning that PASTIS must sample over a wider parameter space when computing the marginal likelihood of each scenario. While ensuring that all possible parameter combinations for each scenario are considered, this method requires significantly more time to run for a given target than VESPA does.

Each of the aforementioned procedures was designed to work with minimal information about a given target star in order to argue for the existence of a transiting planet around it. This design mainly grew out of necessity, as information about many planet candidate hosts and the region of sky in which they were located was sparse in the absence of additional observations. For instance, the number of stars within each pixel was often unknown, and the stars that were known were not always precisely characterized. These facts imposed limitations on the functionalities of the procedures. Specifically, they restricted testable false-positive scenarios to those involving the target star and a single unresolved star, even though there could have been a multitude of unknown stars in the group of pixels used to extract a given light curve. Additionally, poorly characterized target stars forced these procedures to use stellar models and isochrone interpolation to estimate host star properties, which comes at the cost of computation time.

These design features make previous validation algorithms poorly optimized for use on planet candidates identified by the Transiting Exoplanet Survey Satellite (TESS; Ricker et al. 2010). TESS differs from Kepler by being an all-sky survey that focuses on the nearest and brightest stars in order to find planets that are well suited for mass measurement and atmospheric characterization. However, this increased sky coverage comes at the cost of resolution. The TESS cameras

contain pixels that span $21''$, which means that each pixel covers an area of sky roughly $25\times$ larger than those utilized by Kepler. Because of this, the assumption that there is at most one additional star contributing to the flux in a given aperture is unlikely to be true. In addition to scenarios involving a bound stellar companion or a chance alignment of a nonassociated star near the target star, a TESS validation procedure must be capable of considering false-positive scenarios involving a multitude of known stars near a given target.³² While tools like VESPA have been used to validate planet candidates detected by TESS after ruling out false positives due to nearby stars with supplementary follow-up observations (e.g., Cloutier 2019; Günther et al. 2019; Quinn et al. 2019; Vanderspek et al. 2019; Cloutier et al. 2020; Eisner et al. 2020; Gilbert et al. 2020; Huang et al. 2020), no tool exists as of yet that can perform a multistar analysis on its own.

Luckily, the drawback of decreased resolution is counteracted by the wealth of information on nearby stars provided by the second Gaia data release (DR2; Brown et al. 2018). DR2 provides optical photometry, astrometry, and positions for over 1 billion of the nearest stars in the Galaxy. Perhaps most importantly, it is reported that DR2 consistently resolves individual point sources that reside more than $2''/2$ apart, which allows for the identification of stars blended within a TESS pixel to levels previously only possible with supplementary follow-up. With this knowledge, one can test for false-positive scenarios around known nearby stars and conduct more precise centroid analyses. In addition, the focus on nearby and bright stars means that most TESS planet candidate hosts can be more easily characterized using archival and follow-up data. In fact, the properties of millions of TESS targets have already been compiled in the TESS Input Catalog (TIC; Stassun et al. 2018). It would benefit a validation procedure for TESS planet candidates to leverage these known stellar properties, rather than use stellar models to estimate them.

In this work, we present TRICERATOPS (Tool for Rating Interesting Candidate Exoplanets and Reliability Analysis of Transits Originating from Proximate Stars), a new Bayesian tool formulated to validate and vet TESS planet candidates.³³ The procedure calculates the probabilities of a wide range of transit-producing scenarios using the primary transit of the planet candidate, preexisting knowledge of its host and nearby stars, and the current understanding of planet occurrence and stellar multiplicity.

Our tool is designed to provide fast³⁴ and accurate calculations that can be used not only to validate transiting planet candidates, as validation tools have been used to do in the past, but also to serve as a metric for ranking targets of follow-up programs. Because a majority of TESS targets will be bright enough to be followed up with ground-based telescopes, there will inevitably be more planet candidate hosts to observe from the ground than time and resources allow for. We therefore encourage the use of our tool to identify targets that would benefit most from additional vetting.

³² It should be noted that because TESS focuses on brighter stars than Kepler did and the field density of brighter stars is low compared to the field density of fainter stars, most of these contaminating stars will contribute only a small fraction of the total flux within the pixel. By contrast, stars blended within a Kepler pixel had a higher probability of having comparable brightnesses.

³³ Available at <https://github.com/stevengiacalone/triceratops>.

³⁴ Typical run time of about 5 minutes on a standard two-core laptop for a single target.

The layout of this paper is as follows. In Section 2 we present our vetting and validation procedure, including how we determine the possible scenarios for a given target star, and calculate the probability of each. In Section 3 we present detailed statistical validation results for a confirmed planet and for a known false positive. In Section 4 we present the results of our calculations for a sample of 68 TOIs that are known planets or false positives, conduct a performance assessment, and define the criteria a TOI must meet in order to be validated. In Section 5 we report observations that identify several TOIs as false positives originating from nearby stars and compare these observations with TRICERATOPS predictions. In Section 6 we apply our tool to 384 unclassified TOIs and statistically validate 12. In Section 7 we provide a discussion of our results, provide suggestions for how our tool can best be utilized, and present features that we plan on implementing in the future. Lastly, we provide concluding remarks in Section 8.

2. Procedure

Our validation procedure is initiated when the user inputs the ID of a target star listed in the TESS Input Catalog (TIC) that has a transiting planet candidate. Using the MAST module of `astroquery` (Ginsburg et al. 2019), the tool queries the TIC for all stars within a circle of radius 10 pixels from the target. The positions, TESS magnitudes, and available stellar properties of each star are recorded for later use. Next, the user is required to specify the aperture used to extract the TESS light curve for each sector in which the target was observed. The remaining steps of the procedure are summarized as follows:

1. TRICERATOPS calculates the proportion of flux contributed to the aperture by each star near the target. Using the user-entered transit depth, the algorithm identifies the stars bright enough to produce the observed transit-like signal.
2. Using the user-entered primary transit of the planet candidate and light-curve models of transiting planets and eclipsing binaries, TRICERATOPS calculates the marginal likelihood of each transit-producing scenario.
3. Given the marginal likelihood and prior probability of each scenario, the algorithm calculates the probability of each scenario.
4. The algorithm uses these probabilities to determine whether the planet candidate can be classified as a validated planet, a likely planet, or a likely nearby false positive.

2.1. Flux Ratio Calculation

Initially, each star within 10 pixels of the target is considered a potential origin of the transit-like event. Because each star is contributing a different amount of flux to the aperture, the size that the transiting object must be to produce the observed transit depth is different for each star. Because the transiting object size is important for determining the probability of each scenario, the relative flux contributed by each star in the aperture is essential information.

We calculate the flux ratio contributed by each star using a method similar to that used in Stassun et al. (2018) to determine the contamination ratios reported for candidate target stars in the TIC. Specifically, we assume that the point-spread function (PSF) of each star takes the form of a circular 2D Gaussian

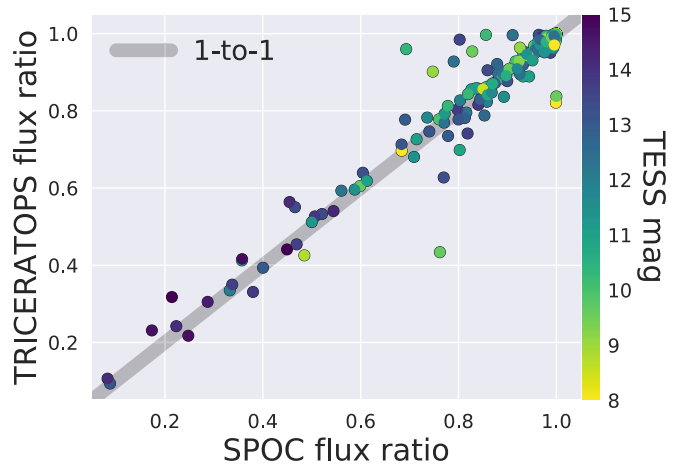


Figure 1. Comparison of target star flux ratios (i.e., the fraction of the flux in the aperture due to the target star) reported by TRICERATOPS and the TESS SPOC pipeline for 228 TOIs. A 1-to-1 line is also shown for illustrative purposes. The two methods yield consistent results, with slightly larger discrepancies for brighter stars.

where the area under each Gaussian (i.e., the total flux) is determined using the TESS magnitudes reported in the TIC. We estimate the standard deviation of the Gaussian using the TESS pixel response function (PRF) models on MAST.³⁵ Due to effects relating to the design of the TESS optics, the exact PRF for a star is dependent on the location on the CCD on which it is observed. These models allow one to estimate the PRF for a given star by providing the size and shape of the TESS PRF at 25 locations on each CCD. We fit each PRF model to a circular 2D Gaussian and record the best-fit standard deviation, finding that it typically ranges between 0.6 and 0.9 pixels. For simplicity, we adopt a standard deviation of 0.75 pixels for all stars, regardless of CCD location. For each star, we integrate the flux in the aperture and divide by the total flux contributed to the aperture by all stars to determine its flux ratio, X_s . For targets that are observed in multiple sectors, we assume that the flux ratio for a given star is the average of its flux ratios across each sector.

To ensure that our method provides reliable flux ratios, we compare in Figure 1 the target star flux ratios for 228 TOIs obtained using our method with those reported by the TESS Science Processing Operations Center (SPOC) pipeline (Jenkins et al. 2016), which calculates flux ratios using the actual PRF models discussed above.³⁶ Both of these calculations are carried out with the aperture used by the TESS SPOC pipeline to extract the light curve of the target star. The figure shows good agreement between the two calculations, with a slightly better agreement for fainter stars.

After flux ratios are determined, we eliminate stars that are too faint to be the source of the observed dimming event. If the observed transit depth is δ_{obs} , the relative transit depth for each star is simply $\delta_s = \delta_{\text{obs}}/X_s$. For stars that contribute relatively little flux to the aperture, it is possible for δ_s to exceed unity. We exclude these stars from further analysis.

³⁵ <https://archive.stsci.edu/missions-and-data/transiting-exoplanet-survey-satellite-tess>

³⁶ Note that the decision to use Gaussian models rather than the actual TESS PRFs for our calculation was made in the interest of computational expediency.

Table 1
Scenarios Tested by TRICERATOPS

Scenario	Configuration	Parameter Vector, θ_j
TP	No unresolved companion; transiting planet with P_{orb} around target star	(i, R_p)
EB	No unresolved companion; eclipsing binary with P_{orb} around target star	(i, q_{short})
EBx2P	No unresolved companion; eclipsing binary with $2 \times P_{\text{orb}}$ around target star	(i, q_{short})
PTP	Unresolved bound companion; transiting planet with P_{orb} around primary star	$(i, R_p, q_{\text{long}})$
PEB	Unresolved bound companion; eclipsing binary with P_{orb} around primary star	$(i, q_{\text{short}}, q_{\text{long}})$
PEBx2P	Unresolved bound companion; eclipsing binary with $2 \times P_{\text{orb}}$ around primary star	$(i, q_{\text{short}}, q_{\text{long}})$
STP	Unresolved bound companion; transiting planet with P_{orb} around secondary star	$(i, R_p, q_{\text{long}})$
SEB	Unresolved bound companion; eclipsing binary with P_{orb} around secondary star	$(i, q_{\text{short}}, q_{\text{long}})$
SEBx2P	Unresolved bound companion; eclipsing binary with $2 \times P_{\text{orb}}$ around secondary star	$(i, q_{\text{short}}, q_{\text{long}})$
DTP	Unresolved background star; transiting planet with P_{orb} around target star	$(i, R_p, \text{simulated star})$
DEB	Unresolved background star; eclipsing binary with P_{orb} around target star	$(i, q_{\text{short}}, \text{simulated star})$
DEBx2P	Unresolved background star; eclipsing binary with $2 \times P_{\text{orb}}$ around target star	$(i, q_{\text{short}}, \text{simulated star})$
BTP	Unresolved background star; transiting planet with P_{orb} around background star	$(i, R_p, \text{simulated star})$
BEB	Unresolved background star; eclipsing binary with P_{orb} around background star	$(i, q_{\text{short}}, \text{simulated star})$
BEBx2P	Unresolved background star; eclipsing binary with $2 \times P_{\text{orb}}$ around background star	$(i, q_{\text{short}}, \text{simulated star})$
NTP	No unresolved companion; transiting planet with P_{orb} around nearby star	(i, R_p)
NEB	No unresolved companion; eclipsing binary with P_{orb} around nearby star	(i, q_{short})
NEBx2P	No unresolved companion; eclipsing binary with $2 \times P_{\text{orb}}$ around nearby star	(i, q_{short})

2.2. Transit Scenario Identification

After calculating the flux ratio for each star in the aperture, we determine the scenarios that can produce the observed transit-like event. Our procedure considers a total of 15 scenarios for the target star and an additional three scenarios for each nearby star with $\delta_s < 1$. These scenarios are summarized in Table 1.

The 15 target star scenarios can be classified into three configurations. The first is the case where the target star has no unresolved stellar companion (where we define ‘‘companion’’ to encompass both bound and foreground/background stars). In this case, we consider the scenarios of a transiting planet with the reported orbital period around the target star (TP), an EB with the reported orbital period around the target star (EB), and an EB with twice the reported orbital period around the target star (EBx2P). The last of these scenarios is meant to capture the possibility that the observed transit is caused by eclipsing binary stars of roughly equal size, such that the primary and secondary eclipses are mistaken for the primary transit of a smaller object with half the orbital period. The second configuration is that in which the target star has an unresolved bound stellar companion. In this case, we consider the scenarios of a transiting planet around the target star with the reported orbital period (primary TP, or PTP), an eclipsing binary with the reported orbital period around the target star (primary EB, or PEB), an eclipsing binary with twice the reported orbital period around the target star (primary EBx2P, or PEBx2P), a transiting planet with the reported orbital period around the companion (secondary TP, or STP), an eclipsing binary around the companion (secondary EB, or SEB), and an eclipsing binary with twice the reported orbital period around the companion (secondary EBx2P, or SEBx2P). The third configuration is that in which there is an unresolved foreground or background star along the line of sight to the target star. In this case, we again consider the scenarios of a transiting planet with the reported orbital period around the target star (diluted TP, or DTP), an eclipsing binary with the reported orbital period around the target star (diluted EB, or DEB), an eclipsing binary with twice the reported orbital period around the target star (diluted EBx2P, or DEBx2P), a transiting planet with the

reported orbital period around the companion (background TP, or BTP), an eclipsing binary with the reported orbital period around the companion (background EB, or BEB), and an eclipsing binary with twice the reported orbital period around the companion (background EBx2P, or BEBx2P).³⁷

For nearby stars with $\delta_s < 1$, we also consider the scenarios of a transiting planet with the reported orbital period around that star (nearby TP, or NTP), an eclipsing binary with the reported orbital period around that star (nearby EB, or NEB), and an eclipsing binary with twice the reported orbital period around that star (nearby EBx2P, or NEBx2P). Each of these scenarios operates under the assumption that the nearby star has no unresolved stellar companion. These scenarios can also be omitted by the calculation if false positives originating from the respective nearby stars have been ruled out through supplementary follow-up.

2.3. Stellar Property Estimation

Whenever possible, we use the stellar properties listed in the TIC in our calculations. However, for reasons that will be discussed, there are times in our procedure where we must estimate the properties (i.e., mass M_* , radius R_* , and effective temperature T_{eff}) of a star in order to determine the probability of the corresponding scenario. We do so using the empirical and semiempirical relations between stellar properties used to populate these fields in the TIC.

For stars with $M_* > 0.63M_{\odot}$ (corresponding roughly to $T_{\text{eff}} > 4000$ K), we determine stellar properties using the results from Torres et al. (2010a). Using the same method discussed in Section 3 of Stassun et al. (2018), we draw spline curves through the distribution of points in M_*-T_{eff} and M_*-R_* space. For stars with $M_* \leq 0.63M_{\odot}$, we repeat this process using a sample of stars from the specially curated TESS Cool Dwarf Catalog (Muirhead et al. 2018). We select nodal points using the sample such that they are continuous with the curves obtained for hotter stars.

³⁷ The BTP and BEB scenarios also include unresolved foreground stars, but the case where a background star is blended with the target star is typically the relevant one.

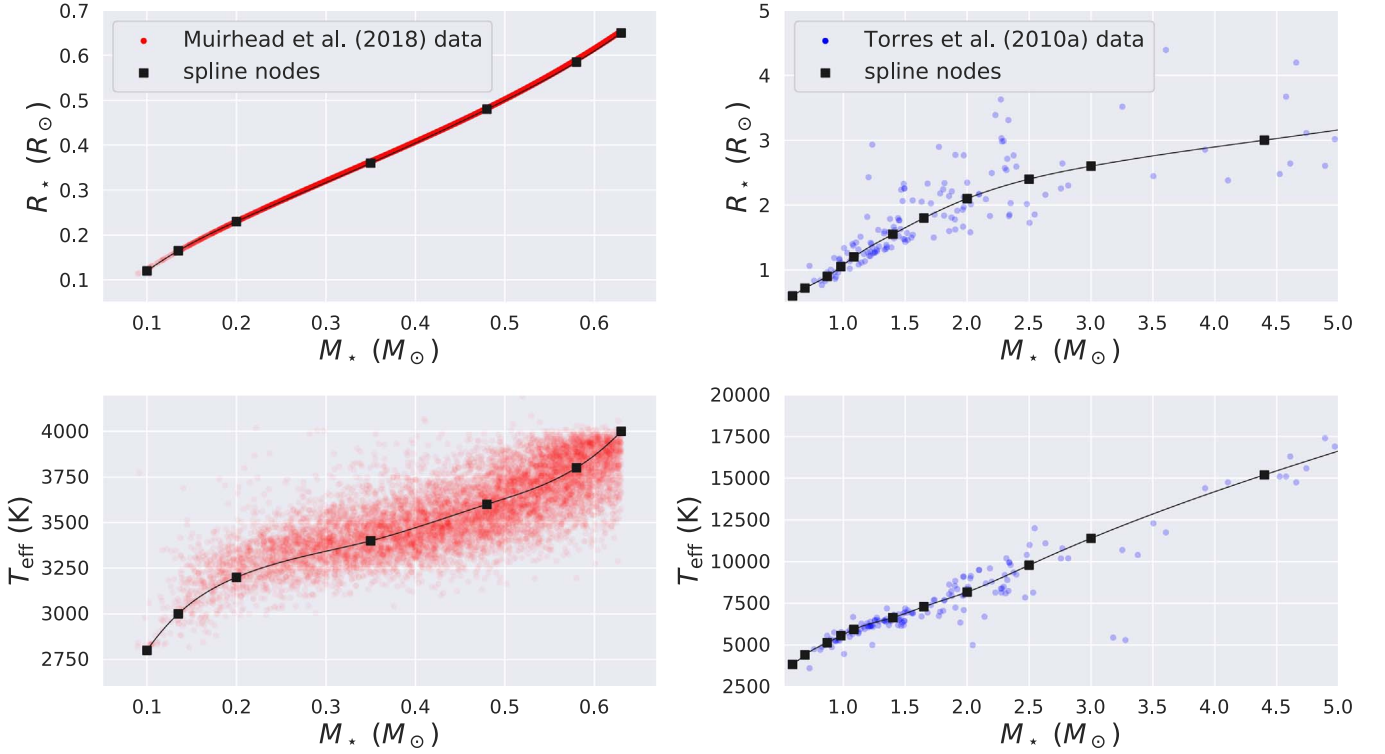


Figure 2. Left: R_* and T_{eff} vs. M_* for stars in the TESS Cool Dwarf Catalog. Red points are stars from the catalog, and black squares are nodes used to draw spline relations through these points. Right: R_* and T_{eff} vs. M_* for the stars reported in Torres et al. (2010a). Blue points are stars from Torres et al. (2010a), and black squares are nodes used to draw spline relations through these points.

The spline curves and the samples on which they are based are shown in Figure 2. The result of this process is a set of relations that allows us to estimate the R_* and T_{eff} of a star given M_* .

2.4. Probability Calculation

We employ a Bayesian framework in our procedure and thus make use of Bayes’s theorem:

$$p(S_j|D) \propto p(S_j)p(D|S_j), \quad (1)$$

where $p(S_j|D)$ is the posterior probability of the j th scenario S_j given the data D , $p(S_j)$ is the prior probability of scenario S_j , and $p(D|S_j)$ is the marginal likelihood of the data D given the scenario S_j (sometimes also referred to as the global likelihood, or the Bayesian evidence). Because we work with a transit model characterized by the parameter vector θ_j , we express the marginal likelihood as the marginalization of the likelihood $p(D|\theta_j, S_j)$ over θ_j :

$$p(D|S_j) = \int p(\theta_j|S_j)p(D|\theta_j, S_j)d\theta, \quad (2)$$

where $p(\theta_j|S_j)$ is the prior distribution of the model parameters. We discuss how these quantities are calculated throughout the remainder of this section.

After calculating $p(S_j|D)$ for each scenario, we determine the relative probability of each scenario using the equation

$$P_j = \frac{p(S_j|D)}{\sum p(S_j|D)}. \quad (3)$$

From here, we define two quantities that are useful for vetting and validation purposes. First, the FPP is given by

$$\text{FPP} = 1 - (\mathcal{P}_{\text{TP}} + \mathcal{P}_{\text{PTP}} + \mathcal{P}_{\text{DTP}}). \quad (4)$$

This quantity represents the probability that the observed transit is due to something other than a transiting planet around the target star. Second, the nearby false-positive probability (NFPP) is given by

$$\text{NFPP} = \sum (\mathcal{P}_{\text{NTP}} + \mathcal{P}_{\text{NEB}} + \mathcal{P}_{\text{NEBx2P}}) \quad (5)$$

(i.e., the sum of all scenarios involving nearby stars). This quantity represents the probability that the observed transit originates from a resolved nearby star rather than the target star.

2.4.1. Scenario Priors

The scenario prior represents the prior probability of a given scenario before the data are considered. The only scenario prior we employ in our calculation is the probability of a transiting planet or eclipsing binary having the P_{orb} applied to the model. For both transiting planets and eclipsing binaries, we assume that the probability distribution of P_{orb} takes the form of a broken power law in the range of 0.1–50 days. Using these probability distributions, we calculate the prior probability of an orbital period P'_{orb} by integrating the probability distribution between $P'_{\text{orb}} - 0.1$ and $P'_{\text{orb}} + 0.1$:

$$p(P'_{\text{orb}}) = \int_{P'_{\text{orb}}-0.1}^{P'_{\text{orb}}+0.1} p(P_{\text{orb}})dP_{\text{orb}}. \quad (6)$$

For transiting planets we base the behavior of this distribution on studies of planet occurrence rates as a function

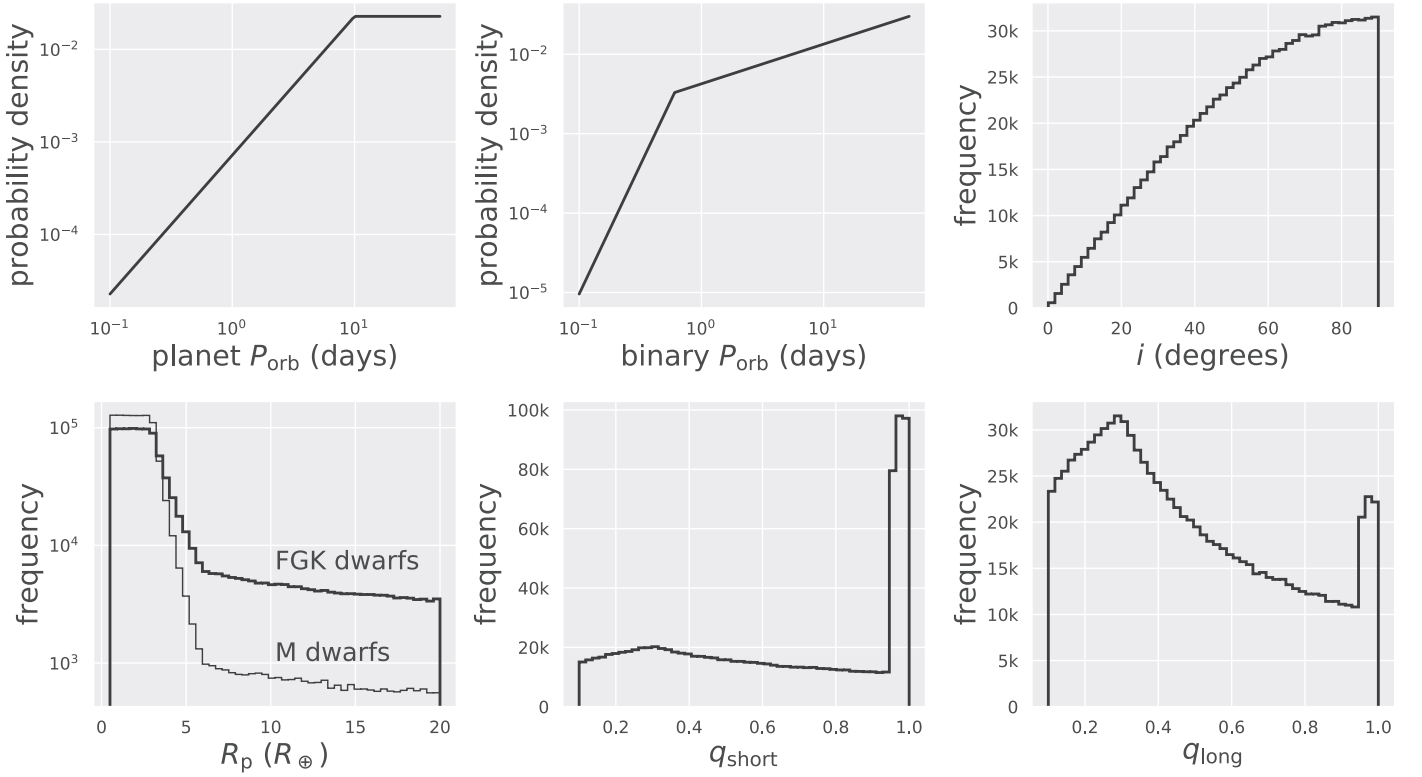


Figure 3. Visualizations of the distributions used to determine model priors and sample parameters in our calculations. Top left: probability density function for the orbital periods of transiting planets. Top middle: probability density function for the orbital periods of eclipsing binaries. Top right: parameter prior distribution for inclination. Bottom left: parameter prior distribution for planet radius. Bottom middle: parameter prior distribution for short-period stellar companion mass ratio. Bottom right: parameter prior distribution for long-period stellar companion mass ratio.

of orbital period (e.g., Howard et al. 2012; Dong & Zhu 2013; Petigura et al. 2013; Dressing & Charbonneau 2015; Mulders et al. 2015a, 2018). We express $p(P_{\text{orb}})$ as a broken power law with a break at $P_{\text{orb}} = 10$ days and the form

$$p(P_{\text{orb}}) \sim \begin{cases} P_{\text{orb}}^{1.5} & 0.1 \text{ days} \leq P_{\text{orb}} \leq 10 \text{ days} \\ P_{\text{orb}}^{0.0} & 10 \text{ days} < P_{\text{orb}} \leq 50 \text{ days} \end{cases} \quad (7)$$

Note that while planet occurrence is typically expressed as a nonseparable function of both planet radius and P_{orb} , we treat the two variables as independent in our calculation procedure.

For eclipsing binaries we base the behavior of this distribution on the results of the Kepler Eclipsing Binary Catalog (Kirk et al. 2016), which contains the properties of thousands of objects that were classified as EBs based on their light-curve morphologies. After correcting the catalog for eclipsing binaries that were not detected owing to orbital misalignment, we find that $p(P_{\text{orb}})$ is best expressed as a broken power law with a break at $P_{\text{orb}} = 0.3$ days and the form

$$p(P_{\text{orb}}) \sim \begin{cases} P_{\text{orb}}^{5.0} & 0.1 \text{ days} \leq P_{\text{orb}} \leq 0.3 \text{ days} \\ P_{\text{orb}}^{0.5} & 0.3 \text{ days} < P_{\text{orb}} \leq 50 \text{ days} \end{cases} \quad (8)$$

It is common for validation procedures to also include priors that capture the overall planet occurrence and stellar multiplicity rate. Planet occurrence rate studies have revealed that the probability of an FGKM dwarf hosting a planet with $P_{\text{orb}} < 50$ days ranges from 10% to 100%, decreasing as a function of increasing host star mass (e.g., Fressin et al. 2013; Petigura et al. 2013; Dressing & Charbonneau 2015). Stellar multiplicity rate

studies have determined that the probability of an FGKM dwarf hosting a stellar companion with $P_{\text{orb}} < 50$ days ranges from 1% to 10%, increasing as a function of increasing host mass (Moe & Di Stefano 2017). This implies that all scenarios involving transiting planets should have a prior probability 10–100 \times higher than those involving eclipsing binaries. At first, we included this prior in the algorithm. However, after testing the performance of our tool on known transiting planets and astrophysical false positives (see Section 4), we concluded that the prior gave transiting planet scenarios too much of an advantage. This advantage often caused an underestimation of FPP, which led the algorithm to classify astrophysical false positives as transiting planets. To avoid this apparent bias, we omit these priors from our calculation procedure.

2.4.2. Parameter Prior Distributions

Every scenario we test is associated with a vector θ_j of parameters that are needed for modeling the light curves of each scenario. The parameters that compose these vectors for each scenario are shown in Table 1. To reflect the fact that certain values of these parameters are more common than others, each is associated with a probability distribution. In this section, we define each of these parameters and their respective probability distributions. Examples of these distributions are shown in Figure 3 for a sample size of 10^6 .

The parameter i represents the inclination of the orbit of a transiting planet or eclipsing binary. Assuming an isotropic distribution of orbits, the distribution of inclinations takes

the form

$$p(i) \sim \sin i. \quad (9)$$

The parameter R_p represents the radius of a transiting planet. Because this distribution is known to be dependent on host star mass, we use different distributions for M dwarfs and FGK dwarfs. The two distributions differ in the prevalence of giant planets ($R_p > 6R_\oplus$), which are known to be less common around M dwarfs than they are around their more massive counterparts by a factor of ~ 10 (e.g., Dressing & Charbonneau 2013; Fressin et al. 2013; Petigura et al. 2013; Mulders et al. 2015b). We express these distributions as broken power laws with breaks at $R_p = 3R_\oplus$ and $R_p = 6R_\oplus$ and a range of $R_p = 0.5R_\oplus - 20R_\oplus$ (e.g., Mulders et al. 2015b, 2018).³⁸ For M dwarfs the distribution takes the form

$$p(R_p) \sim \begin{cases} R_p^{0.0} & 0.5R_\oplus \leq R_p \leq 3R_\oplus \\ R_p^{-7.0} & 3R_\oplus < R_p \leq 6R_\oplus \\ R_p^{-0.5} & 6R_\oplus < R_p \leq 20R_\oplus \end{cases}, \quad (10)$$

and for FGK dwarfs the distribution takes the form

$$p(R_p) \sim \begin{cases} R_p^{0.0} & 0.5R_\oplus \leq R_p \leq 3R_\oplus \\ R_p^{-4.0} & 3R_\oplus < R_p \leq 6R_\oplus \\ R_p^{-0.5} & 6R_\oplus < R_p \leq 20R_\oplus \end{cases}. \quad (11)$$

The parameter q_{short} represents the mass ratio between the host star and a short-period stellar companion (i.e., an eclipsing binary). To calculate this distribution, we extrapolate from the results of Moe & Di Stefano (2017) for Sun-like stars. In the study, q is parameterized as a broken power law with a break at $q = 0.3$ and a range of $q = 0.1 - 1.0$. In addition, the parameterization takes into account the excess of stellar “twins” (stellar companions with $q > 0.95$) with a term $\mathcal{F}_{\text{twin}}$ (defined as the fraction of stars with $q > 0.3$ that have $q > 0.95$) that boosts the prevalence of these stars in the probability distribution. For short-period stellar companions, the distribution takes the form

$$p(q_{\text{short}}) \sim \begin{cases} q_{\text{short}}^{0.3} & 0.1 \leq q \leq 0.3 \\ q_{\text{short}}^{-5.0} & 0.3 < q \leq 1.0 \end{cases} \quad (12)$$

with $\mathcal{F}_{\text{twin}} = 0.3$.

The parameter q_{long} represents the mass ratio between the target star and a long-period stellar companion (i.e., an unresolved bound companion). Again, we utilize the parameterization and extrapolate results of Moe & Di Stefano (2017) for Sun-like stars. For long-period stellar companions, the distribution takes the form

$$p(q_{\text{long}}) \sim \begin{cases} q_{\text{long}}^{0.3} & 0.1 \leq q \leq 0.3 \\ q_{\text{long}}^{-0.95} & 0.3 < q \leq 1.0 \end{cases} \quad (13)$$

with $\mathcal{F}_{\text{twin}} = 0.05$.

The parameter “simulated star” represents the properties of a star drawn from a population of stars simulated with TRILEGAL. To determine the properties of blended stars used in DTP, DEB, DEBx2P, BTP, BEB, and BEBx2P scenarios,

we simulate a population of stars in a 0.1 deg^2 region of the sky centered at the target star. We then produce a distribution of possible foreground/background stars by removing all stars with TESS magnitudes brighter than the target and fainter than 21, which typically yields between 300 and 1000 stars. When simulating an instance of these scenarios, we draw a star directly from this distribution.

2.4.3. Marginal Likelihoods

Because the integral in Equation (2) is typically impossible to solve analytically, it is common to approximate the integral by sampling $p(\theta_j | S_j)$. This is, in fact, what is done when calculating odds ratios between competing scenarios in the PASTIS and VESPA validation procedures. In this work, we calculate the marginal likelihood using arithmetic mean estimation (Kass & Raftery 1995). This method allows us to calculate the marginal likelihood using Monte Carlo sampling by approximating Equation (2) as

$$p(D|S_j) \sim \frac{1}{N} \sum_{n=1}^N p(D|\theta_j^{(n)}, S_j), \quad (14)$$

where $\theta_j^{(n)}$ is the n th sample from the parameter prior distribution and N is the total number of samples. This is typically regarded as the simplest estimator of the marginal likelihood, but it is often avoided because it can produce a large variance in $p(D|S_j)$ if N is not sufficiently high and is relatively inefficient when integrating over a large number of parameters. We take two approaches to combat these drawbacks: (1) we chose an N high enough to produce results that are consistent between consecutive calculations (which we determine to be $N = 10^6$), and (2) we make simplifying assumptions in our transiting planet and eclipsing binary models that minimize the number of parameters we must marginalize over.

The first simplifying assumption we make is to assume that the M_* , R_* , and T_{eff} of each resolved star are known precisely. Unless the user provides these parameters, they are assumed to be equal to those listed in the TIC. In addition, any other stars added to our transit model that do not have estimates for these quantities (e.g., eclipsing binaries or unresolved companions) are assumed to be precisely characterized based on their M_* (see Section 2.3). Because the transit models are sensitive to these parameters, this assumption saves us from having to marginalize over a distribution of target star properties.

The second simplifying assumption we make is to assume a fixed orbital period and zero eccentricity (e) in all scenarios considered, which significantly simplifies the orbital solution of the system. There is strong evidence that short-period planets are biased toward lower e (e.g., Kane et al. 2012; Kipping 2013; Shabram et al. 2016). According to the NASA Exoplanet Archive,³⁹ 84% of confirmed planets with $P_{\text{orb}} < 30$ days and reported eccentricities have $e < 0.2$. The same justification can be applied to short-period eclipsing binaries. Moe & Di Stefano (2017) showed that the e distribution of binary stars with $P_{\text{orb}} < 10$ days goes like $e^{-0.8}$. This implies that 72% of short-period eclipsing binaries have $e < 0.2$. Because a majority of TOIs will have $P_{\text{orb}} < 30$ days (due to the ~ 27 -day intervals in which sectors are observed and the general requirement for at least two transits be observed for a system to become a planet

³⁸ Note that we do not model the gap in the radius distribution between $1.5R_\oplus$ and $2.0R_\oplus$ (Fulton et al. 2017).

³⁹ <https://exoplanetarchive.ipac.caltech.edu/>

candidate), we believe that the assumption of circular orbits is justified in most cases. However, users of TRICERATOPS should be aware that this assumption becomes less valid as longer orbital periods are considered.

We calculate $p(D|\theta_j^{(n)}, S_j)$ as the product of two terms:

$$p(D|\theta_j^{(n)}, S_j) = p(D_{\text{tra}}|\theta_j^{(n)}, S_j) \times w^{(n)}, \quad (15)$$

where the first term is the likelihood of the transit data and $w^{(n)}$ is a weight that encapsulates our ability to rule out unresolved companions near the target star using high-resolution imaging follow-up. This weight is intended to decrease the likelihood of scenarios involving unresolved companions when stronger constraints on the existence such companions are applied.

The likelihood of the transit data is calculated using the equation

$$p(D_{\text{tra}}|\theta_j^{(n)}, S_j) \propto \prod \exp \left[-\frac{1}{2} \left(\frac{y_l - f(t_l|\theta_j^{(n)})}{\sigma} \right)^2 \right], \quad (16)$$

where y_l is the flux of the l th data point, $f(t_l|\theta_j^{(n)})$ is the flux given by the model for the parameter vector $\theta_j^{(n)}$ at the time of the l th data point, and σ is the characteristic uncertainty of the flux.

For PTP, PEB, PEBx2P, STP, SEB, and SEBx2P scenarios we calculate $w^{(n)}$ using Equation (23) of Moe & Di Stefano (2017). Equation (23) of Moe & Di Stefano (2017) provides the frequency of bound stellar companions as a function of primary mass and orbital period. We calculate this quantity for the n th sample of the parameter prior distribution using the following steps: (1) determine magnitude difference between the primary and secondary star using the mass of the target and the n th draw of q_{long} , (2) use the contrast curve obtained from high-resolution imaging to determine the angular separation beyond which the simulated secondary would have been detected, (3) convert this angular separation to an orbital period using the parallax of the target and the masses of the target and simulated secondary, and (4) use this orbital period and Equation (23) of Moe & Di Stefano (2017) to calculate the corresponding frequency of bound stellar companions. If no high-resolution imaging data are available to fold in, the angular separation used in step (2) is assumed to be $2''2$ (Brown et al. 2018).

For DTP, DEB, DEBx2P, BTP, BEB, and BEBx2P scenarios we calculate $w^{(n)}$ using the results of the TRILEGAL simulation discussed in Section 2.4.2. Specifically, we calculate this likelihood as the frequency of unresolved foreground and background stars aligned with the target star in the sky. This calculation is performed with the following steps: (1) determine the magnitude difference between the target star and the n th drawn foreground/background star, (2) use the contrast curve obtained from high-resolution imaging to determine the angular separation beyond which the simulated foreground/background star would have been detected, (3) use this separation and the total number of simulated stars to estimate the frequency of unresolved foreground/background stars near the target. As for the previous scenarios, if no high-resolution imaging data are available to fold in, the angular separation used in step 2 is assumed to be $2''2$ (Brown et al. 2018).

We set the maximum value of $w^{(n)}$ for each scenario to 1. We also set $w^{(n)} = 1$ for TP, EB, EBx2P, NTP, NEB, and NEBx2P scenarios, which do not involve unresolved companions.

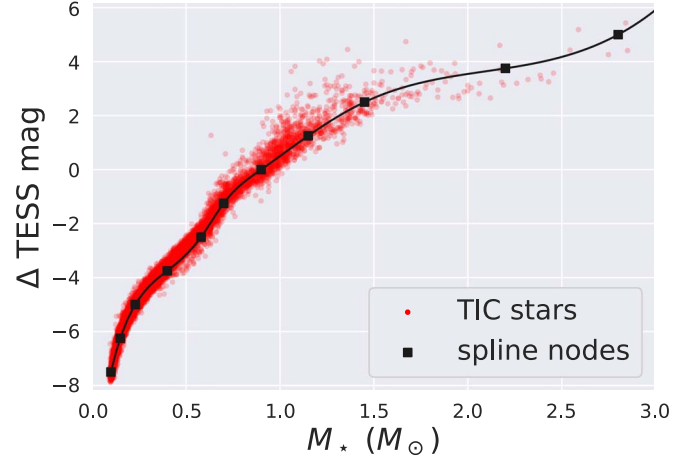


Figure 4. Δ TESS magnitude between a star of mass M_* and a 10th magnitude, $1M_\odot$ star. Red points are stars queried from the TIC located between 99 and 101 pc away. Black squares are the nodes of the spline relation used to calculate the TESS mag of unresolved stars modeled in our calculations.

2.4.4. Light-curve Modeling

We calculate Equation (16) by modeling light curves using a modified version of *batman* (Kreidberg 2015). Here we describe the steps that go into simulating the transits of each scenario.

The simplest scenario to model is the TP scenario, in which we assume that all of the flux originates from the host star. For this scenario, we use *batman* in its default form. For this scenario, as well as all other scenarios, we use quadratic limb-darkening coefficients chosen based on the T_{eff} and $\log g$ of the host star (Claret 2018).

For all scenarios involving eclipsing binaries, we must account for the fact that the flux is split between the host star and the short-period companion. Doing so requires an estimate for the flux contributed by the eclipsing binary, which we find by determining a relation between M_* and TESS magnitude. We begin by querying the TIC for all stars located a distance between 99 and 101 pc away. We then draw a spline curve through the distribution of points in the TESS magnitude— M_* plane, which is shown in Figure 4. This relation allows us to calculate the TESS band flux ratio between two stars given their masses and adjust the in-transit flux of the light curve accordingly.

For scenarios involving unresolved companions, we again must account for the flux dilution from the additional star. For scenarios involving an unresolved bound companion (whose mass is determined by q_{long}), we use the spline relation shown in Figure 4 to determine the flux contribution of the star. For scenarios involving an unresolved foreground/background star, we use the TESS magnitude provided by TRILEGAL to determine the flux contribution of the star.

Lastly, we apply constraints to our transit models for all “EB” and “EBx2P” scenarios. For the former, we require $q_{\text{short}} < 0.95$ and for the expected secondary eclipse depth to be shallower than $1.5\times$ the scatter of the TESS light-curve flux (otherwise the secondary eclipse would have been detected and identified as such). For the latter, we require $q_{\text{short}} > 0.95$. If the n th model light curve does not satisfy these conditions, we set the likelihood of the transit to zero.

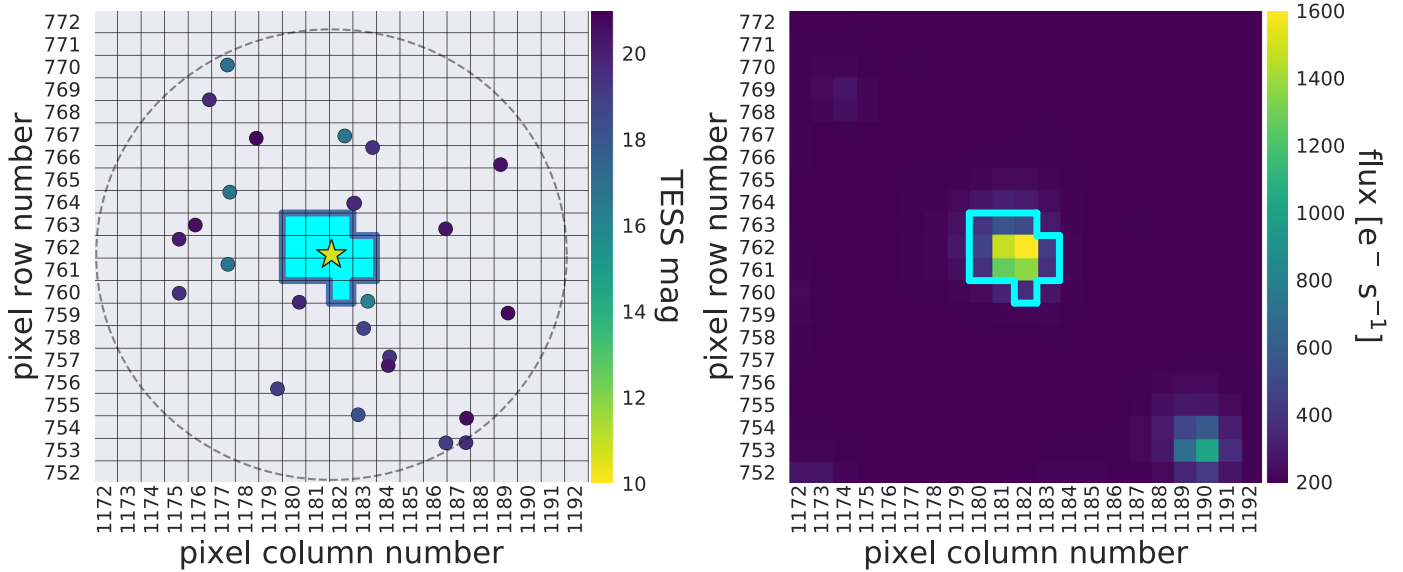


Figure 5. Visualization of TIC querying for TOI 465.01 (TIC 270380593). Left: all stars within 10 pixels of the target star (the limits of which are approximated by the black dashed line). The target star is located in the center pixel and is indicated by a star symbol. The aperture used to extract the light curve is highlighted in blue. Right: time-averaged TESS image of the same pixels, with the same aperture overlaid.

3. Examples

For illustrative purposes we display here each step of our calculation for two TOIs, one of which has been confirmed as a transiting planet and one of which has been ruled out as a nearby eclipsing binary.

3.1. TIC 270380593 (TOI 465.01)

We apply our algorithm on the previously confirmed TOI 465.01 (WASP-156b; Demangeon et al. 2018), a $\sim 6R_{\oplus}$ planet orbiting a K dwarf with a 3.84-day orbital period. The host star, which has a TESS magnitude of 10.73 and is located 122 pc away, was observed with a 2-minute cadence in sector 4.

We begin by searching for all other stars within 10 pixels of the target star. This is shown in Figure 5, where the location of each nearby star relative to the local TESS pixels is shown on the left and the corresponding TESS image is shown on the right. Next, we calculate the flux contribution of each star and determine which contribute enough flux to the aperture to produce a transit with the reported depth. In this case, the target star is the only star bright enough to host the signal. We therefore ignore NTP, NEB, and NEBx2P scenarios for the remainder of this analysis, which leaves 15 scenarios to be considered.

Next, we determine the best-fit model parameters for each of the 15 scenarios considered. The results of this step are displayed in Figure 6 and Table 2. Figure 6 shows the best-fit transit models for each scenario compared to the extracted TESS light curve. Table 2 shows the best-fit values for several transit model parameters. We see in both of these that the best-fitting scenario is the TP scenario.

The final step in the procedure is to calculate the relative probability of each scenario using Equation (3). These probabilities are shown in the rightmost columns of Table 2. For this TOI, we find that FPP = 0.33 and NFPP = 0.0.

The above calculation was done assuming that unresolved companions near the target star can be ruled out beyond $2''$. However, if one is able to further constrain the separation beyond which an unresolved star could exist, this number can

be decreased to that new separation. On 2019 July 10, we obtained adaptive optics (AO) assisted high-resolution images of this TOI with ShARCS/ShaneAO on the Shane 3 m telescope at Lick Observatory, shown in Figure 7. These images were reduced using the steps outlined in Hirsch et al. (2019) and Savel et al. (in preparation), to which we refer the reader for more information. With these observations, we produce a contrast curve (also shown in Figure 7) that can be folded into the TRICERATOPS analysis in order to further constrain the probabilities of scenarios involving unresolved companions.

To show how this changes the results of our tool, we repeat the calculation with this constraint applied. The impact that this AO follow-up has on the probability of each scenario is shown in the rightmost column of Table 2, which now yields FPP = 0.19.

3.2. TIC 438490744 (TOI 529.01)

We also apply our algorithm on TOI 529.01, a candidate with a 1.67-day orbital period that has been ruled out as an NEB around the nearby star TIC 438490748 (see Section 5 for more details). The originally proposed host star is an M dwarf with a TESS magnitude of 14.14 and a distance of 63 pc away. This TOI was observed with a 2-minute cadence in sector 6.

We again begin by searching for all other stars within 10 pixels of the target star, as shown in Figure 8. After calculating the flux contribution due to each star, it is determined that two nearby stars, TIC 438490736 and TIC 438490748, contribute enough light to the aperture for them to host the observed transit. As a result, there are 21 scenarios to be considered for this TOI.

Figure 9 and Table 3 show the best-fit transits and transit model parameters for these scenarios, respectively. According to these results, the most probable scenario is the NEBx2P scenario around the nearby star TIC 438490748. In fact, the preference for this scenario is so strong that this TOI has FPP > 0.99 and NFPP > 0.99.

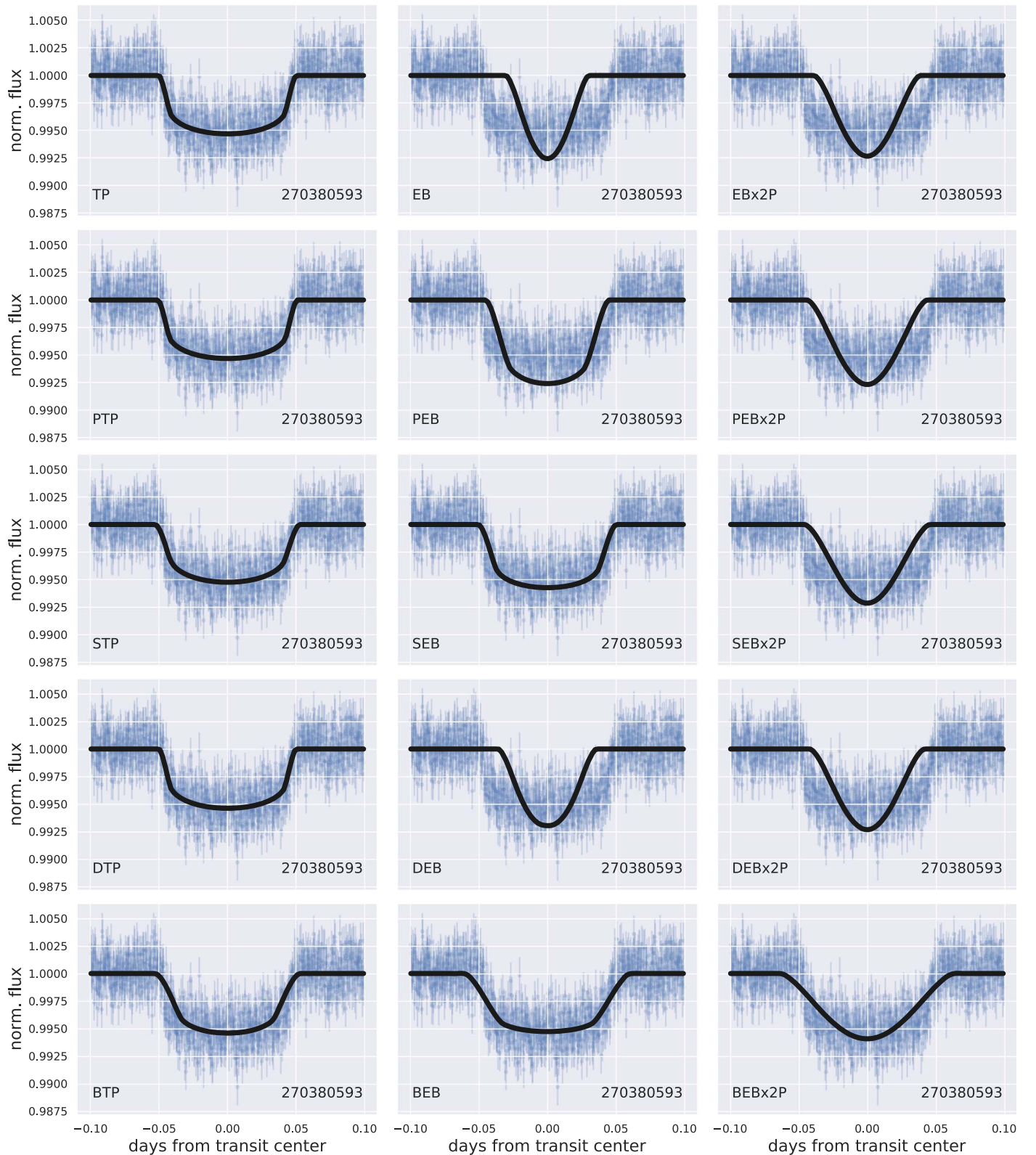


Figure 6. Fit of each transit scenario for TOI 465.01. The purple points are 2-minute cadence TESS data, while the black curves are the best-fit light curves. The scenario being fit for is in the lower left corner of each panel, and the TIC ID of the star being fit for is in the lower right corner of each panel.

4. Planet Vetting and Validation

In this section, we analyze the performance of TRICERA-TOPS by running it on several classified TOIs observed with

both 2-minute cadence and 30-minute cadence observations. Using these results, we define the conditions a TOI must meet to be vetted and validated.

Table 2
Scenario Probabilities for TOI 465.01

Scenario	TIC ID	M_* (M_\odot)	R_* (R_\odot)	P_{orb} (days)	i (deg)	R_p (R_\oplus)	R_{EB} (R_\odot)	\mathcal{P}_j	\mathcal{P}_j with AO
TP	270380593	0.81	0.85	3.84	87.3	6.27		0.39	0.61
EB	270380593	0.81	0.85	3.84	85.3		0.10	<0.01	<0.01
EBx2P	270380593	0.81	0.85	7.67	85.3		0.84	<0.01	<0.01
PTP	270380593	0.81	0.85	3.84	87.4	6.35		0.22	0.14
PEB	270380593	0.81	0.85	3.84	86.4		0.10	<0.01	<0.01
PEBx2P	270380593	0.81	0.85	7.67	85.4		0.83	<0.01	<0.01
STP	270380593	0.79	0.82	3.84	87.8	8.71		0.31	0.19
SEB	270380593	0.63	0.65	3.84	89.8		0.10	0.01	<0.01
SEBx2P	270380593	0.48	0.49	7.67	87.3		0.49	<0.01	<0.01
DTP	270380593	0.81	0.85	3.84	87.5	6.26		0.06	0.06
DEB	270380593	0.81	0.85	3.84	85.7		0.10	<0.01	<0.01
DEBx2P	270380593	0.81	0.85	7.67	85.3		0.83	<0.01	<0.01
BTP	270380593	0.55	0.48	3.84	89.3	19.36		<0.01	<0.01
BEB	270380593	0.81	0.75	3.84	89.7		0.19	<0.01	<0.01
BEBx2P	270380593	0.83	1.01	7.67	85.4		0.85	<0.01	<0.01
TIC ^a	270380593	$0.81^{+0.10}_{-0.10}$	$0.85^{+0.06}_{-0.06}$						
WASP-156b ^b	270380593	$0.84^{+0.05}_{-0.05}$	$0.76^{+0.03}_{-0.03}$		$89.1^{+0.6}_{-0.9}$	$5.72^{+0.22}_{-0.22}$			

Notes.

^a Host star properties from version 8 of the TIC (Stassun et al. 2018).

^b Best-fit host star and planet properties from Demangeon et al. (2018).

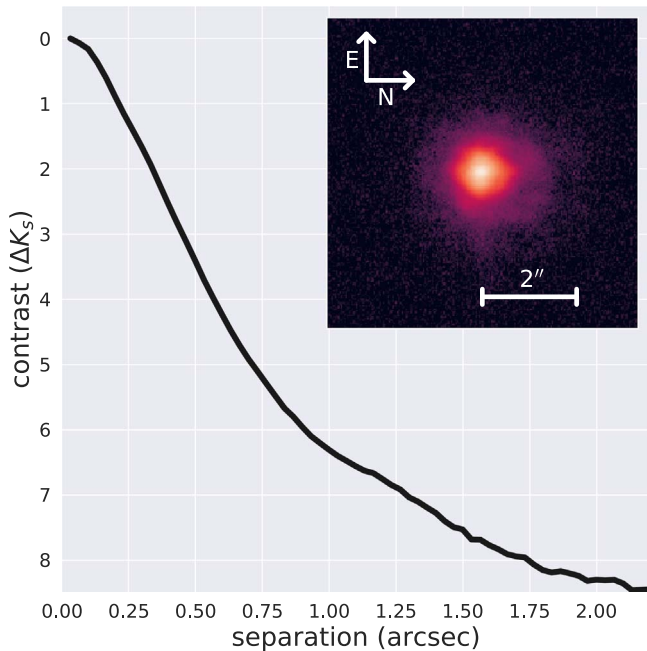


Figure 7. High-resolution image of TOI 465 obtained with ShARCS/ShaneAO in K_s band and corresponding contrast curve.

4.1. 2-minute Cadence Data

We begin by running our code on TOIs identified in 2-minute cadence data collected by TESS. In the first 2 yr of the TESS mission, these observations were collected for $\sim 200,000$ nearby dwarf stars across nearly the entire sky. These observations are processed by the TESS Science Processing Operations Center (SPOC) pipeline (Jenkins et al. 2016), which identifies TCEs and generates data validation reports that contain information useful for further vetting. These stars are then subjected to manual vetting by the TESS

Science Office to compile a set of TOIs that consist of the TCEs with the best chances of being actual planets.

We use publicly available information from the TESS Follow-up Observation Program (TFOP) website⁴⁰ and 2-minute cadence TESS light curves from MAST to obtain the phase-folded light curves and apertures that we input into TRICERATOPS for each TOI. Because a key function of our algorithm is the identification of TOIs that are false positives around nearby stars, we use light curves extracted using simple aperture photometry instead of those processed with the pre-data-conditioning step of the SPOC pipeline, which removes contamination and variability originating from nearby stars. In order to recreate the conditions under which one would use our tool on new TOIs, we only use data from the first sector in which each TOI is observed and restrict the analysis to TOIs with at least three transits.

In order to have a ground truth with which to compare the results of our algorithm, we restrict our sample of TOIs to those that have been designated as confirmed planets (CPs) and those that have been designated as false positives (FPs) by the TFOP. We also discard TOIs that have been designated FPs due to instrumental false alarms (which our tool does not test for); TOIs without estimates for M_* , R_* , and T_{eff} in the TIC; and TOIs for which we are unable to feasibly recover a transit with the purported orbital parameters. Lastly, we only include planets with best-fit planet radii $R_p < 8R_\oplus$ under the TP scenario. This radius corresponds roughly to the minimum radius of a brown dwarf (e.g., Sorahana et al. 2013) and has been used as an upper limit in the size of objects that can be validated in past validation studies (e.g., Mayo et al. 2018), due to the fact that giant planets, brown dwarfs, and low-mass stars are typically indistinguishable based on radius alone. This leaves 68 TOIs in total, 28 of which are confirmed planets and 40 of which are false positives. The system properties of these TOIs are displayed in Figure 10.

⁴⁰ <https://exofop.ipac.caltech.edu/tess/index.php>

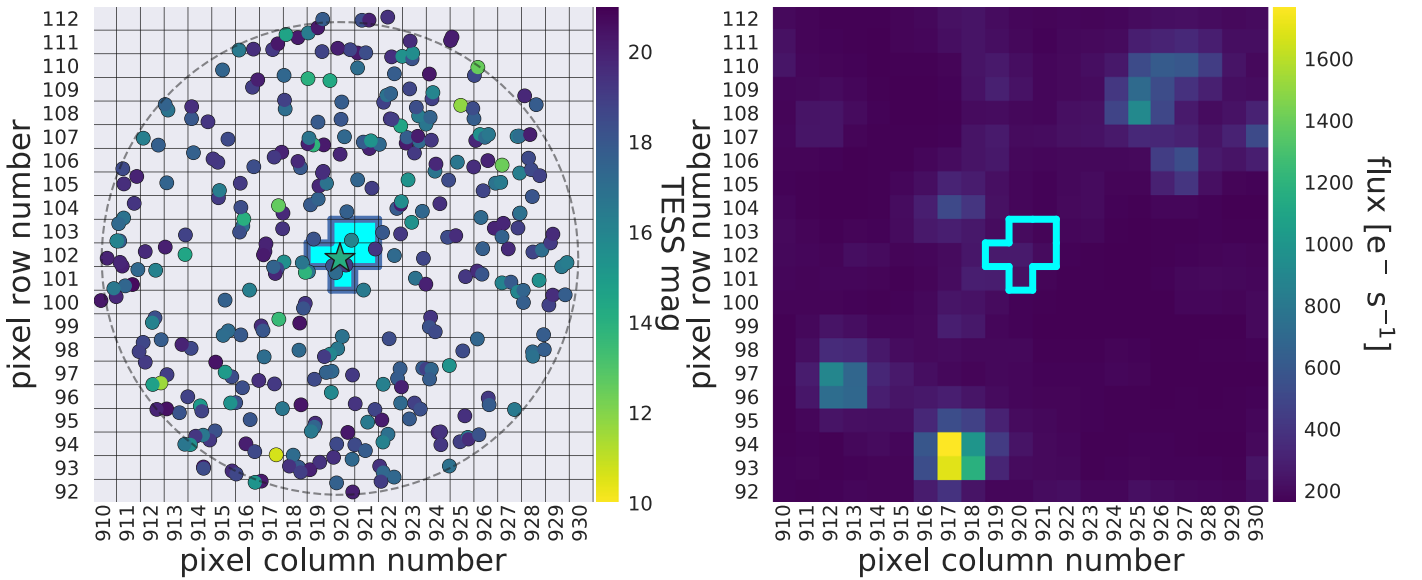


Figure 8. Visualization of TIC querying for TOI 529.01 (TIC 438490744). Left: all stars within 10 pixels of the target star (the limits of which are approximated by the black dashed line). The target star is located in the center pixel and is indicated by a star symbol. The aperture used to extract the light curve is highlighted in blue. Right: time-averaged TESS image of the same pixels, with the same aperture overlaid.

After generating light curves for these TOIs, we calculate the FPP and NFPP for each to determine the limits within which TRICERATOPS can be used reliably. First, we explore how our predictions depend on the signal-to-noise ratio (S/N) of the data. We define the S/N as

$$S/N = \frac{\delta_{\text{obs}}}{\sigma_{\text{CDPP}}} \sqrt{n_{\text{tra}}}, \quad (17)$$

where δ_{obs} is the observed transit depth (i.e., not corrected for dilution from nearby stars), σ_{CDPP} is the combined differential photometric precision (CDPP; Christiansen et al. 2012) of the 2-minute cadence data, and n_{tra} is the number of observed transits. We calculate σ_{CDPP} by applying the `estimate_cdpp` method of `lightkurve` (Lightkurve Collaboration et al. 2018) over the duration of the transit. Because this quantity incorporates our confidence in the size of a transiting object and the overall density of data points in-transit, it should correlate with the ability of TRICERATOPS to characterize the shape of a given transit.

The results of this analysis are shown in Figure 11. For both CPs and FPs, TRICERATOPS generally has more accurate predictions when S/N is higher. Specifically, FPP alone does not appear to be a reliable predictor of TOI disposition when $S/N < 15$, where FPs are frequently assigned low values of FPP that would ideally be reserved for CPs.

Second, we explore how our algorithm performs when NFPP is also considered. Figure 12 shows the distribution of the TOIs in NFPP–FPP space for $S/N < 15$ (on the left) and $S/N > 15$ (on the right). In the figure, we differentiate TOIs that are CPs, TOIs that have been ruled out as FPs around nearby stars (nearby false positives, or NFPs), and TOIs that have been ruled out as FPs originating from the immediate vicinity of the target star (target false positives, or TFPs). The most salient feature of this figure is the region defined by $\text{NFPP} < 10^{-3}$ and $\text{FPP} < 0.5$ that contains nearly all of the CPs, contains none of the NFPs or TFPs, and is independent of S/N. We designate TOIs that exist within this region as likely planets.

Another visible feature of Figure 12 is the pileup of CPs in the region defined by $\text{NFPP} < 10^{-3}$ and $\text{FPP} < 0.05$. Because this region is representative of TOIs with the best chances of being bona fide planets, we use it as a guide in defining our criteria for validating planets. Typically, the standard for validating planets (e.g., with VESPA) is to achieve an FPP below 1%. We therefore define validated planets as TOIs with $\text{NFPP} < 10^{-3}$ and $\text{FPP} < 0.015$ (or $\text{FPP} \leq 0.01$, when rounding to the nearest percent).

As a cross-check of our definition of a validated planet, we calculate the FPP of the TOIs in Figure 12 using VESPA. We run VESPA using the coordinates, stellar photometry (TESS mag, B_{mag} , V_{mag} , J_{mag} , H_{mag} , and K_{mag}), T_{eff} , $\log g$, and parallax listed for each TOI in the TIC. We use the same transit data used in our TRICERATOPS runs and assume a maximum unresolved star separation of $2''$. The FPPs obtained with VESPA are compared to the FPPs obtained with TRICERATOPS in Figure 13. According to the figure, TOIs that score a low FPP with TRICERATOPS generally score a similar FPP with VESPA. When it comes to FPs, and NFPs in particular, TRICERATOPS typically assigns higher FPPs than VESPA does. This is a reflection of our calculation procedure, which considers each star that contributes flux to the target aperture as a potential source of the observed transit. One might also note that there are a few NFPs that are scored low FPPs with both tools. However, because of our condition that a TOI have $\text{NFPP} < 10^{-3}$ to be classified as a validated planet or a likely planet, TRICERATOPS would not identify these candidates as planets. Conversely, because VESPA explicitly requires the assumption that no contaminating stars exist within a specified radius of the target star, it could classify these candidates as planets if all nearby stars are not ruled out as transit sources prior to the analysis. To avoid outcomes like this, VESPA requires a separate calculation of the probability that the transit originates from the target star prior to its FPP calculation (e.g., Morton et al. 2016).

It is also worth noting that the calculation procedures between the tools are not identical. An important difference is that TRICERATOPS takes into account the STP scenario,

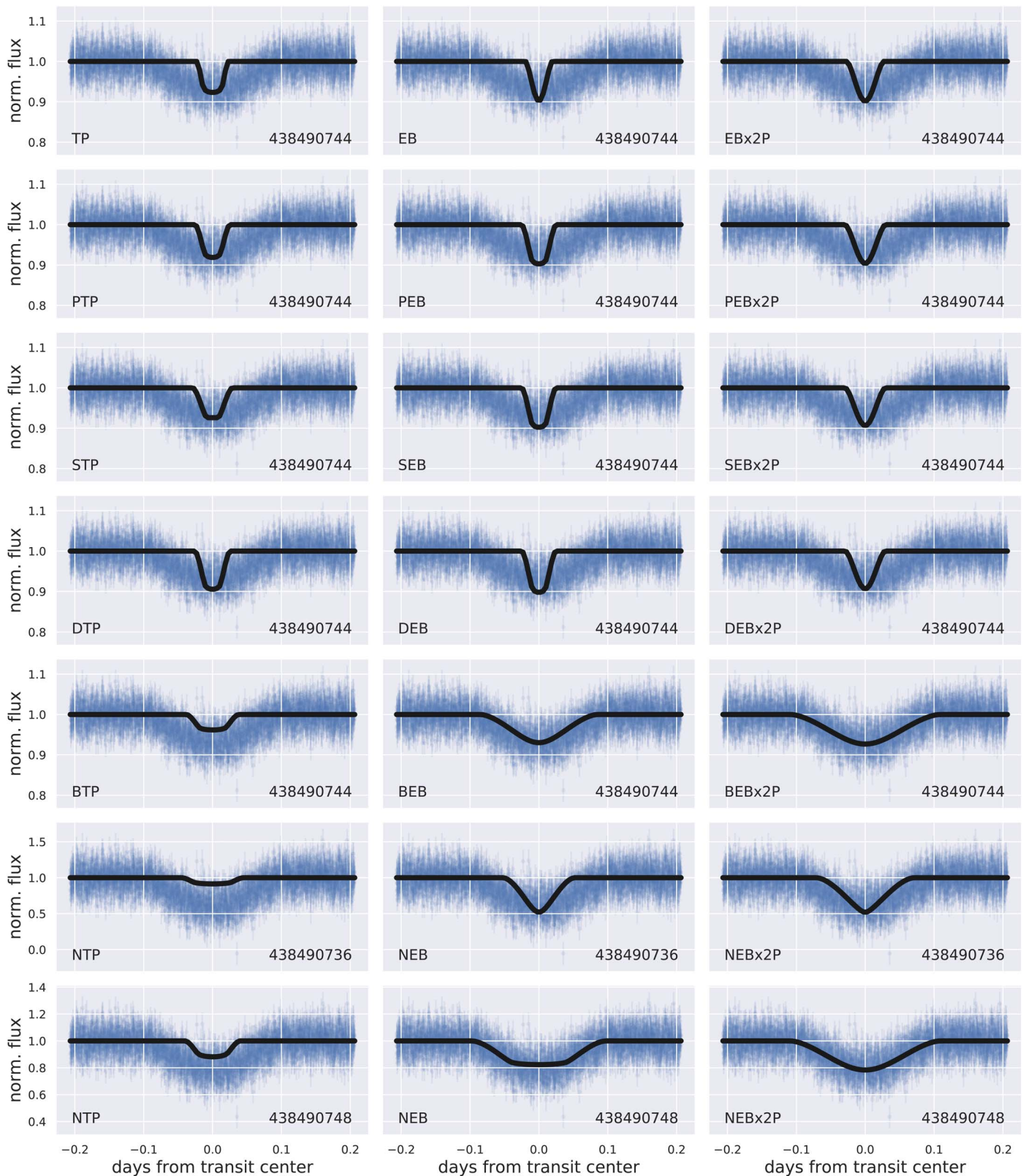


Figure 9. Fit of each transit scenario for TOI 529.01. The purple points are 2-minute cadence TESS data, while the black curves are the best-fit light curves. The scenario being fit for is in the bottom left of each panel, and the TIC ID of the star being fit for is in the bottom right of each panel.

which involves a planet transiting an unresolved bound companion, whereas *VESPA* does not. This false-positive scenario typically has a nonnegligible probability of being the ground truth and therefore inflates the FPP obtained with

TRICERATOPS relative to that of *VESPA*. To test how this impacts the FPP comparison, we calculate the *TRICERATOPS* FPP for each TOI both using (left panel of Figure 13) and omitting (right panel of Figure 13) the STP scenario. We see

Table 3
Scenario Probabilities for TOI 529.01

Scenario	TIC ID	M_* (M_\odot)	R_* (R_\odot)	P_{orb} (days)	i (deg)	R_p (R_\oplus)	R_{EB} (R_\odot)	\mathcal{P}_j
TP	438490744	0.21	0.24	1.67	89.9	6.89		<0.01
EB	438490744	0.21	0.24	1.67	86.6		0.10	<0.01
EBx2P	438490744	0.21	0.24	3.33	87.3		0.24	<0.01
PTP	438490744	0.21	0.24	1.67	90.0	8.61		<0.01
PEB	438490744	0.21	0.24	1.67	89.5		0.10	<0.01
PEBx2P	438490744	0.21	0.24	3.33	87.7		0.24	<0.01
STP	438490744	0.09	0.10	1.67	89.2	19.70		<0.01
SEB	438490744	0.18	0.22	1.67	89.7		0.10	<0.01
SEBx2P	438490744	0.48	0.24	3.33	87.7		0.24	<0.01
DTP	438490744	0.21	0.24	1.67	89.2	9.82		<0.01
DEB	438490744	0.21	0.24	1.67	89.5		0.10	<0.01
DEBx2P	438490744	0.21	0.24	3.33	87.7		0.24	<0.01
BTP	438490744	0.51	0.45	1.67	89.8	19.92		<0.01
BEB	438490744	1.05	1.42	1.67	89.6		1.05	<0.01
BEBx2P	438490744	0.93	1.67	3.33	84.4		0.97	<0.01
NTP	438490736	0.67	0.69	1.67	89.5	19.94		<0.01
NEB	438490736	0.67	0.69	1.67	88.1		0.56	<0.01
NEBx2P	438490736	0.67	0.69	3.33	89.5		0.69	<0.01
NTP	438490748	0.51	0.45	1.67	89.7	19.98		<0.01
NEB	438490748	1.12	1.75	1.67	89.8		0.76	0.06
NEBx2P	438490748	1.08	1.54	3.33	85.2		1.16	0.94
TIC ^a	438490744	$0.21_{-0.02}^{+0.02}$	$0.24_{-0.01}^{+0.01}$					

Note.

^a Host star properties from version 8 of the TIC (Stassun et al. 2018).

that when this scenario is included, there are several TOIs that score a validation-worthy FPP with VESPA that do not with TRICERATOPS. However, when this scenario is omitted from the calculation, the two tools return more consistent results. This suggests that TRICERATOPS is more conservative when validating TOIs and will oftentimes rely on supplementary follow-up observations to achieve $\text{FPP} \leq 0.01$.

4.2. 30-minute Cadence Data

One might expect our code to have a more difficult time distinguishing CPs from FPs when using data with a longer cadence, as they would yield fewer points with which to characterize the shape of the transit. To test this, we also run our code on 30-minute cadence light curves of the same TOIs. We use *eleanor* (Feinstein et al. 2019) to extract these light curves from TESS Full Frame Images (FFIs) within the same sectors and apertures used to obtain the 2-minute cadence light curves.⁴¹

In Figure 14, we show how S/N affects the new FPP calculations. As in the previous section, TRICERATOPS is able to correctly identify CPs and FPs more frequently when S/N is high, but the correlation is weaker overall. Specifically, the FPPs of CPs are less concentrated near zero here than those calculated with the 2-minute data.

In Figure 15, we reproduce the NFPP versus FPP analysis from the previous section using the 30-minute cadence data. We again see that most CPs are contained within a region defined by $\text{NFPP} < 10^{-3}$ and $\text{FPP} < 0.5$, with very few FPs

also falling within this region. Specifically, the region contains 18 CPs and only 2 FPs. In addition, almost no CPs have an $\text{FPP} > 0.7$ (with the exception of one, which is mistaken for a nearby false positive), which implies that a high FPP is still indicative of actual FPs. We thus again designate TOIs with $\text{NFPP} < 10^{-3}$ and $\text{FPP} < 0.5$ as likely planets. However, unlike the results obtained with the 2-minute cadence data, there does not appear to be a region of parameter space in which planets can be confidently validated. Nonetheless, TRICERATOPS results involving long-cadence TESS data are useful for vetting TOIs and prioritizing them for follow-up observations to further investigate the nature of the signal.

5. Nearby False-positive Identification

In addition to its ability to identify likely planets and validate TOIs, TRICERATOPS is proficient at identifying NFPs. In Figures 12 and 15, TOIs with an $\text{NFPP} > 10^{-1}$ are NFPs 85% and 82% of the time, respectively. Additionally, the region defined by $\text{NFPP} > 10^{-1}$ contains over half of the NFPs in our sample for calculations conducted using both 2-minute and 30-minute data. These results suggest that TRICERATOPS can be used to predict which TOIs are NFPs and to determine which nearby stars have the highest probability of hosting the observed transit. We therefore classify TOIs in this region of parameter space as likely NFPs.

As an additional step to assess the ability of our tool to identify NFPs, we compile a set of observations collected by members of TESS Follow-up Observing Program (TFOP)⁴² Sub Group 1 (SG1) that rule out 30 TOIs as NFPs. The follow-up observations were scheduled using the TESS Transit Finder, which is a customized version of the Tapir

⁴¹ More precisely, we run our code on 67 of the 68 TOIs analyzed in the previous section. We were unable to recover the FFI data for TOI 1796.01 (the TOI with the highest S/N in Figure 11) owing to a bug in *eleanor*, which returns an error claiming that the TOI has not yet been observed upon searching for its data.

⁴² <https://tess.mit.edu/followup>

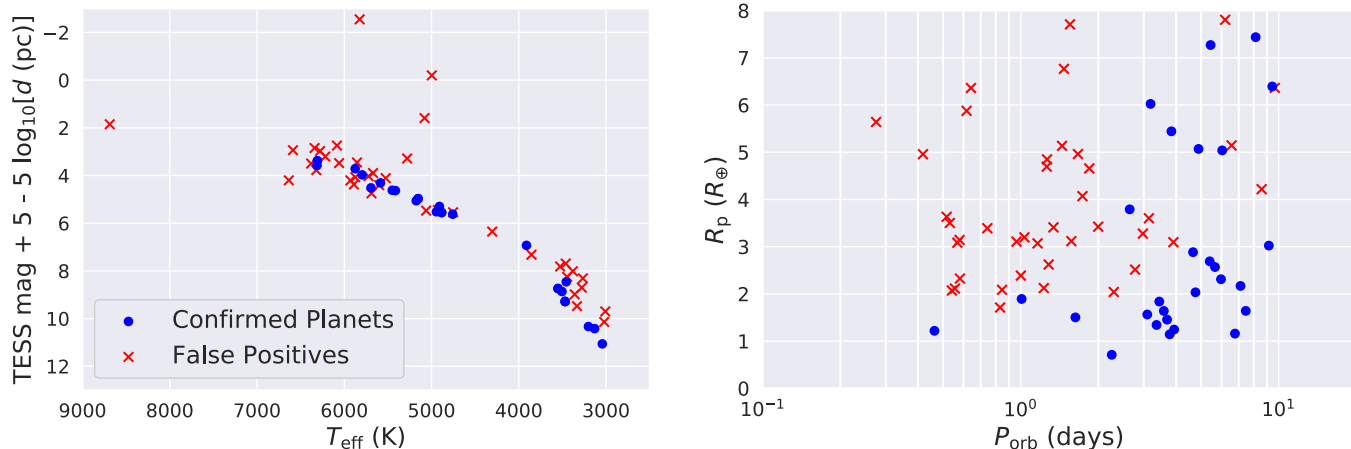


Figure 10. Host star (left) and planet (right) properties of confirmed planets and false positives used in our performance analysis. The sample includes systems with a diversity of host spectral types, planet orbital periods, and predicted planet radii (i.e., the best-fit radii from the TP scenario).

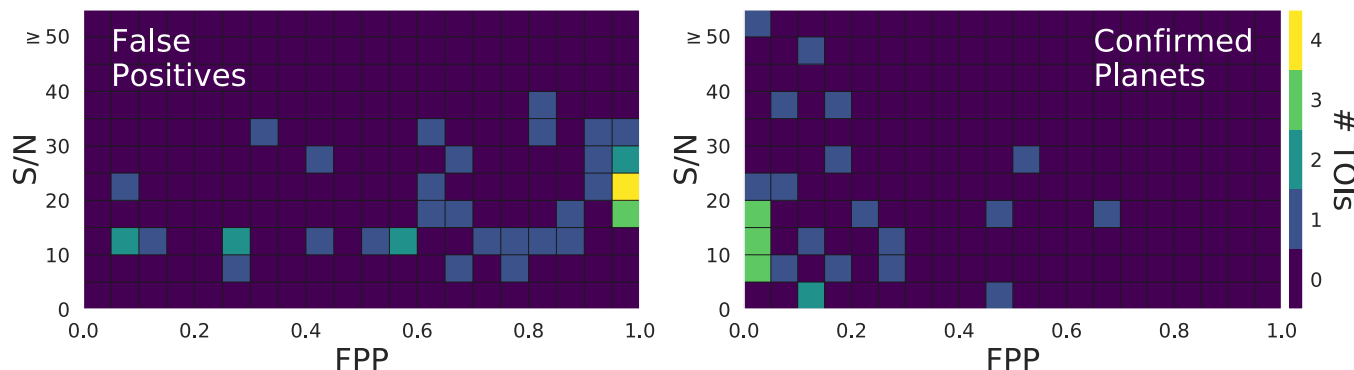


Figure 11. S/N vs. FPP for all false positives (left) and confirmed planets (right) used in our performance analysis. Our tool performs better for TOIs with higher S/Ns. TRICERATOPS performs best when $S/N > 15$.

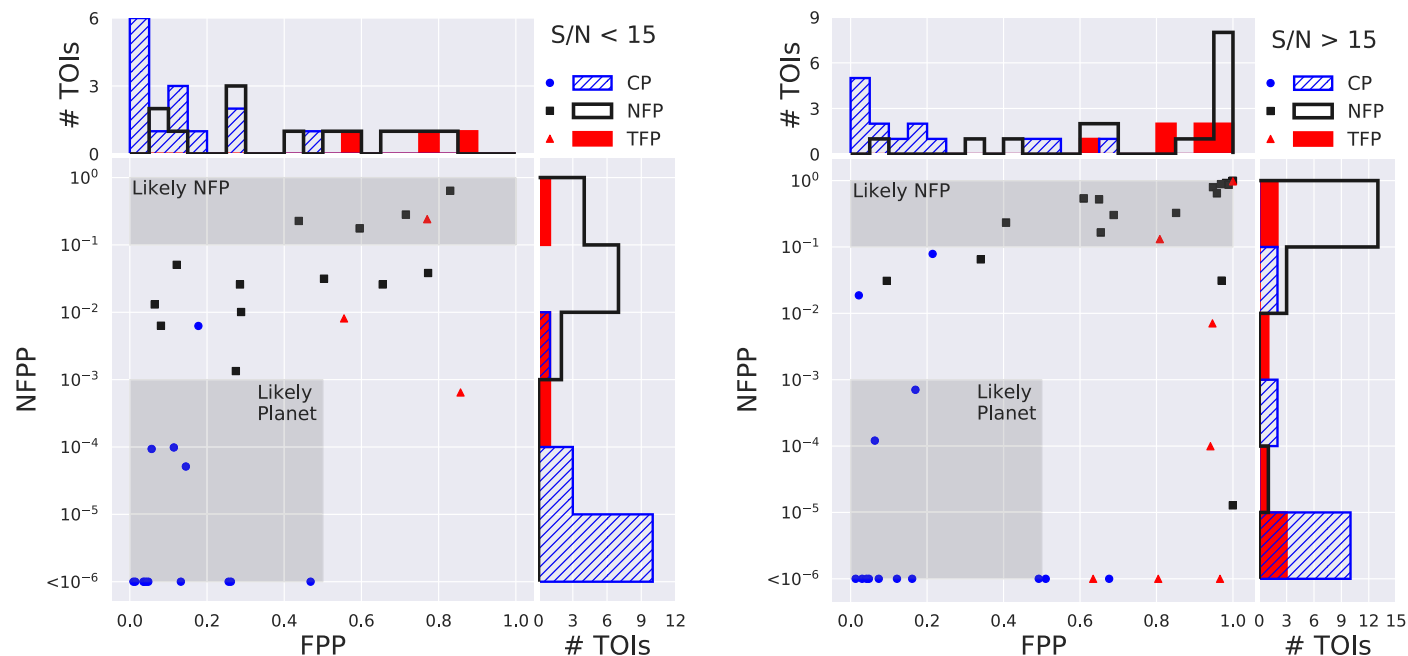


Figure 12. NFPP vs. FPP for $S/N < 15$ (left) and $S/N > 15$ (right). We designate TOIs with $NFPP < 10^{-3}$ and $FPP < 0.5$ as likely planets. For TOIs with $NFPP < 10^{-3}$ and $FPP \leq 0.01$, we are able to rule out FPs with a high enough confidence to consider them validated. Lastly, we are able to identify TOIs that are NFPs with high confidence when $NFPP > 10^{-1}$.

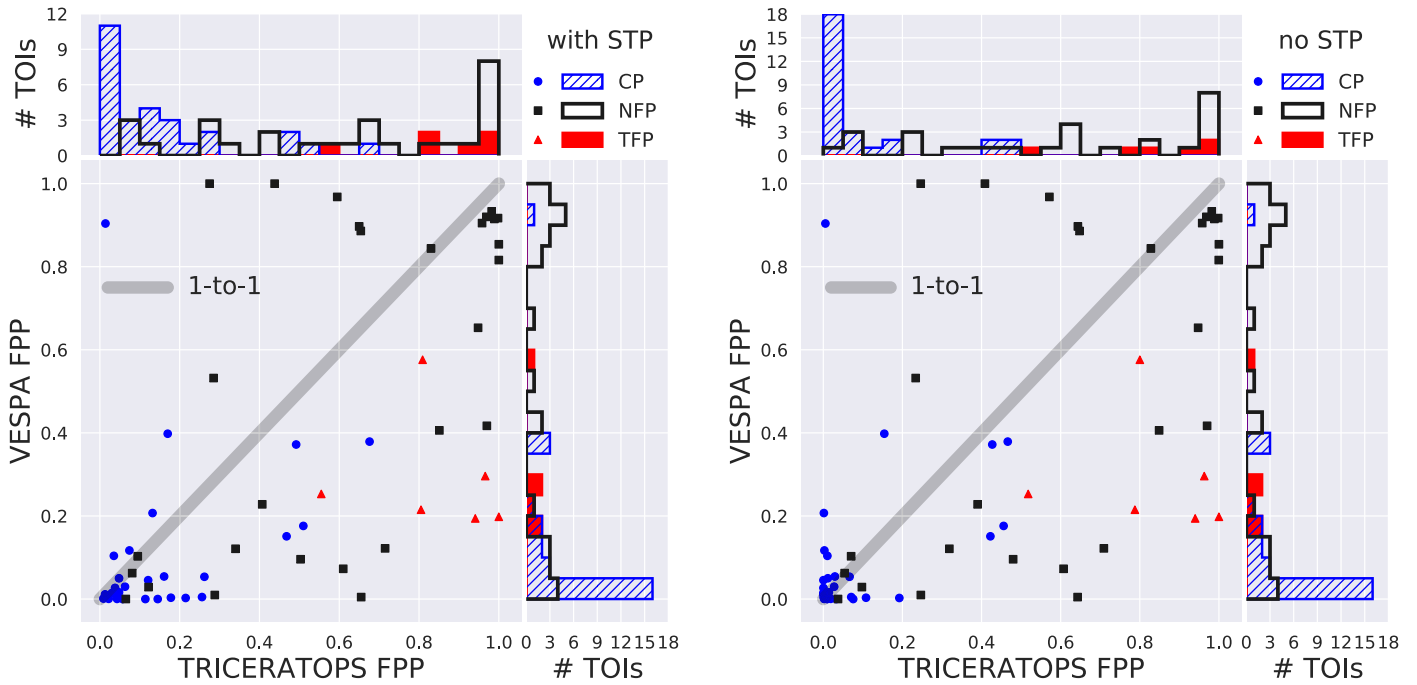


Figure 13. VESPA FPP vs. TRICERATOPS FPP for the TOIs in Figure 12. Left: comparison with the STP scenario included in the TRICERATOPS calculation. Right: comparison without the STP scenario included in the TRICERATOPS calculation. CPs that score a low FPP with TRICERATOPS tend to also score a low FPP with VESPA. This agreement is stronger when the STP scenario (which is not considered in VESPA) is omitted in TRICERATOPS. Conversely, FPs (and in particular, NFPs) generally score higher FPPs with TRICERATOPS than with VESPA owing to the ability of the former to consider nearby stars as potential sources.

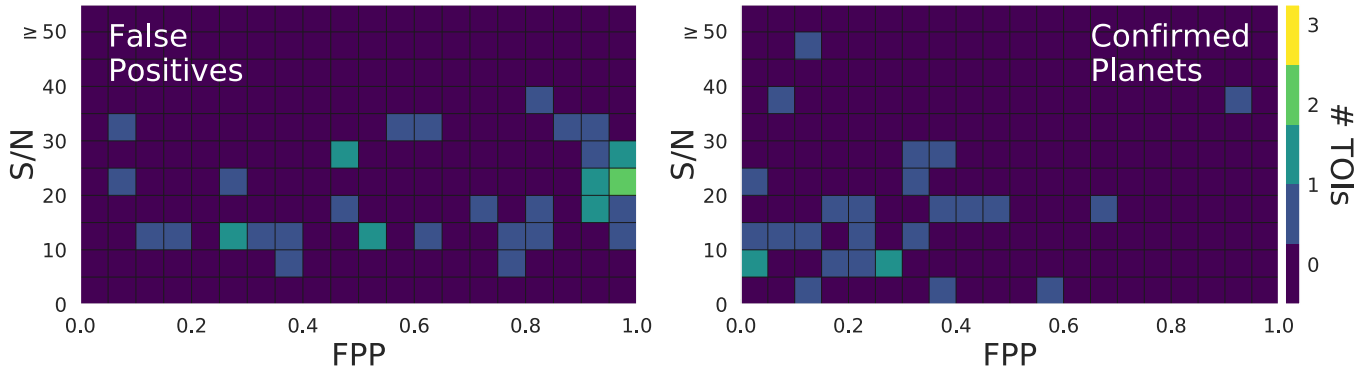


Figure 14. S/N vs. FPP for the same false positives (left) and confirmed planets (right) shown in Figure 11, but calculated using light curves extracted from 30-minute cadence TESS data. While there still appears to be a correlation between S/N and performance, it is less clear here than in Figure 11.

software package (Jensen 2013). Below we outline these observations and compare the empirical results with the NFPs predicted by TRICERATOPS using 2-minute cadence data. A summary of these targets is given in Table 4, and details about the facilities used are given in Table 5.

Another method of discerning NFPs is by searching for centroid offsets in the TESS pixels encompassing a TOI. Oftentimes, the true source of an NFP can be identified using the magnitude and direction of these offsets. In addition to the observations collected by TFOP SG1, we compare our TRICERATOPS predictions with the difference image centroiding analyses for these TOIs in their SPOC data validation reports (Twicken et al. 2018).

With these comparisons, we display that TRICERATOPS often yields similar results to both follow-up observations and predictions made using centroid offsets. For several of these TOIs (17/30), our tool assigns an NFPP high enough to

classify them as likely NFPs. For those that do not meet this criterion, FPP and NFPP are high enough to rule out the possibility of the TOI being a planet. Lastly, in cases where there are several NFP candidates (of which there are 28), TRICERATOPS is frequently (10/28) able to predict which nearby star is the true host of the transit signal.

5.1. TIC 260043723 (TOI 217.01)

TFOP SG1 confirms that the true host of the signal is TIC 260043722. Previous HAT-South data suggested that this TOI is an NEB, which was confirmed by PEST Observatory R_C -band observations with a depth of 200 ppt. This star was also correctly identified as the host of the signal by the SPOC centroid offset analysis. TRICERATOPS identifies two nearby sources other than the target star bright enough to host the signal, one of which is TIC 260043722. The total NFPP calculated by TRICERATOPS is 0.0063. TIC 260043722 has an NFPP of 0.0059,

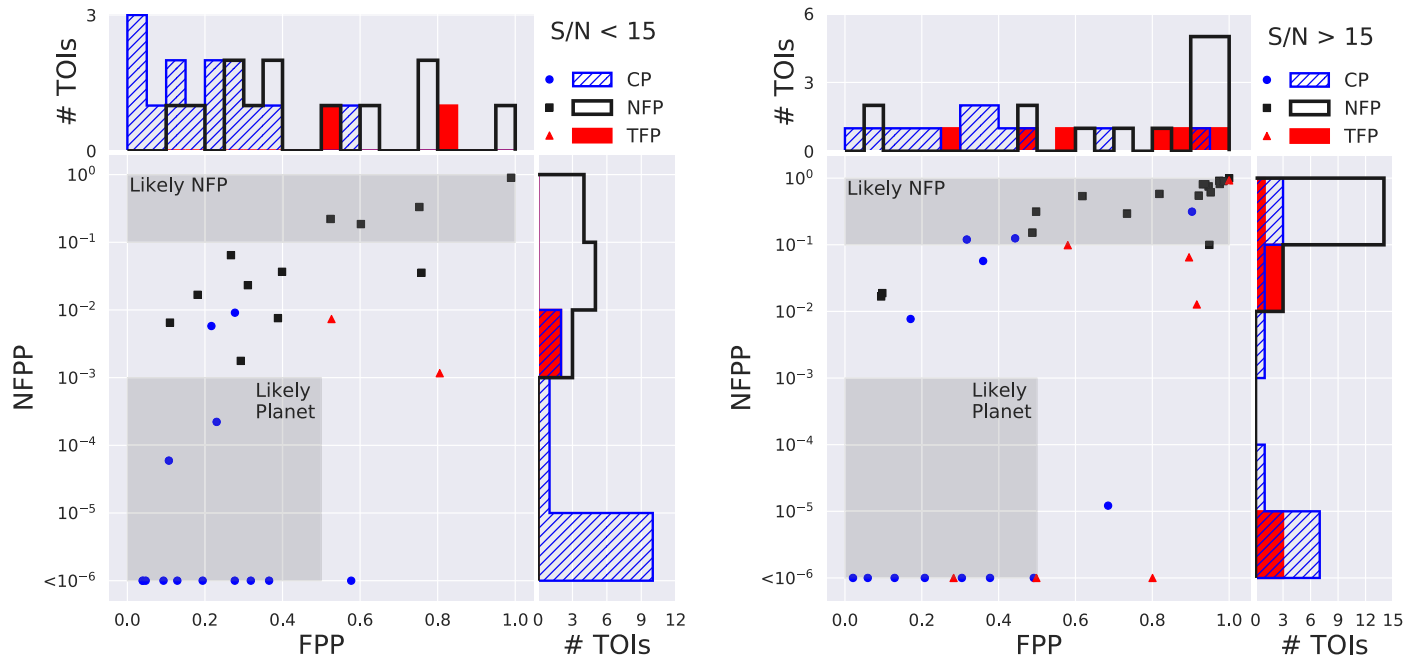


Figure 15. NFPP vs. FPP for $S/N < 15$ (left) and $S/N > 15$ (right), but calculated using 30-minute cadence TESS data. While we are unable to identify a region in which we can validate TOIs, we can still designate TOIs with $NFPP < 10^{-3}$ and $FPP < 0.5$ as likely planets. Additionally, we are still able to identify TOIs that are NFPs with high confidence when $NFPP > 10^{-1}$.

Table 4
TFOP SG1 False-positive Identification Compared to TRICERATOPS Predictions

Target TIC ID	TOI Number	TFOP SG1 Disposition	True Host TIC ID	FPP	Total NFPP	True Host NFPP	# NFP Candidates	True Host Rank
260043723	217.01	NEB	260043722	0.0806	0.0063	0.0059	2	1
279740441	273.01	NEB	279740439	0.6095	0.5377	0.2041	2	2
250386181	390.01	NEB	250386182	0.9703	0.0311	0.0311	2	1
219388773	399.01	NEB	219388775	0.2882	0.0101	0.0101	1	1
176778112	408.01	NEB	176778114	0.3405	0.0650	0.0438	2	1
201781111	467.01	NEB	201781112	0.4065	0.2332	0.1638	3	1
427352241	485.01	NEB	427352247	0.6498	0.5219	0.0693	3	2
108645766	497.01	NEB	108645800	0.8299	0.6361	...	4	...
274138511	506.01	NEB	760244235	0.1215	0.0507	0.0030	10	6
431999925	513.01	NEB	431999916	0.9819	0.9230	0.1482	8	2
438490744	529.01	NEB	438490748	1.0000	0.9938	0.9938	2	1
302895996	531.01	NEB	302895984	0.9477	0.7971	0.0509	5	3
53593457	543.01	NEB	53593470	0.9580	0.6436	...	5	...
59003115	556.01	NEB	59003118	0.2854	0.0258	0.0050	2	2
1133072	566.01	NEB	830310300	0.9687	0.8854	0.0124	9	6
146463781	636.01	NEB	146463868	0.9887	0.8640	...	3	...
432008938	643.01	NEB	432008934	0.9996	0.0001	...	2	...
54085154	662.01	NEB	54085149	0.2747	0.0013	0.0008	2	1
147660201	670.01	NPC	147660207	0.6543	0.1652	0.0868	9	1
391821647	708.01	NEB	~35" W	0.5955	0.1760	...	141	...
373424049	742.01	NEB	373424060	0.4377	0.2268	0.0006	31	23
271596418	868.01	NEB	271596416	0.6551	0.0259	0.0078	7	1
364107753	909.01	NEB	1310226289	0.0645	0.0131	0.0068	4	1
253990973	1061.01	NEB	253985122	0.5030	0.0315	0.0037	9	4
308034948	1206.01	NEB	unknown	0.7727	0.0383	...	108	...
274762761	1256.01	NEB	274762865	0.9981	0.9869	...	6	...
267561446	1284.01	NEB	267561450	0.7151	0.2818	0.0235	13	4
274662200	1285.01	NEB	274662220	0.6880	0.3031	0.0501	21	2
408203470	1289.01	NEB	408203452	0.8512	0.3258	0.1435	10	1
233681149	1340.01	NEB	233681148	0.0947	0.0309	0.0309	1	1

Note. “Total NFPP” is the total NFPP for the TOI. “True Host NFPP” is the NFPP for only the true host of the signal. “# NFP Candidates” is the number of nearby sources bright enough to host the signal. “True Host Rank” is the rank of the true host NFPP, compared to the NFPPs of all other NFP candidates (where a rank of 1 corresponds to the highest NFPP).

Table 5
Facilities Used for TFOP SG1 Follow-up

Observatory	Location	Aperture (m)	Pixel Scale (arcsec)	FOV (arcmin)
Univ. Louisville Moore Obs./CDK20N	Louisville, KY, US	0.51	0.54	37×37
Univ. Louisville Manner Telescope	Mt. Lemmon, AZ, US	0.61	0.39	26×26
Mt. Kent Observatory/CDK700	Toowoomba, Australia	0.7	0.4	27×27
Hazelwood Observatory	Churchill, Victoria, Australia	0.318	0.55	20×13.5
LCOGT 0.4 m	(various)	0.4	0.57	29.2×19.5
LCOGT 1.0 m	(various)	1.0	0.39	26.5×26.5
Fred L. Whipple Obs./MEarth-North	Amado, AZ, USA	0.4	0.76	26×26
Tel. Carlos Sánchez/MuSCAT2	Teide Obs., Tenerife, Spain	1.52	0.44	7.4×7.4
El Sauce Observatory	Coquimbo Province, Chile	0.36	1.47	18.8×12.5
Perth Exoplanet Survey Telescope (PEST)	Perth, Australia	0.3	1.2	31×21
HATNet	(various)	0.11	14	492×492
HAT-South	(various)	0.18	3.7	492×492
TRAPPIST-South	La Silla, Chile	0.6	0.6	22×22
Steward Observatory Phillips Telescope	Mt. Lemmon, AZ, US	0.6	0.38	26×26

making it the most probable NFP host. This NFPP is too low to classify the TOI as a likely NFP and too high to classify the TOI as a likely planet. In addition, the calculated FPP of 0.0806 is too high to classify the TOI as a validated planet.

5.2. TIC 279740441 (TOI 273.01)

TFOP SG1 confirms that the true host of the signal is TIC 279740439. The signal was a nearby planet candidate (signal not on the original TOI, but still possibly planetary) based on observations from the TRAPPIST telescope that show a depth of 40 ppt in a custom $I + z$ -band filter. Later observations with LCOGT (Brown et al. 2013) showed a V -band depth of 30 ppt on the nearby candidate; the wavelength-dependent eclipse depth indicates that it is an eclipsing binary. This star was also correctly identified as the host of the signal by the SPOC centroid offset analysis. TRICERATOPS identifies two nearby sources other than the target star bright enough to host the signal, one of which is TIC 279740439. The total NFPP calculated by TRICERATOPS is 0.5377. TIC 279740439 has an NFPP of 0.2041, making it the second most probable NFP host. This NFPP is high enough to classify the TOI as a likely NFP. In addition, the calculated FPP of 0.6095 is too high to classify the TOI as a likely planet or validated planet.

5.3. TIC 250386181 (TOI 390.01)

TFOP SG1 confirms that the true host of the signal is TIC 250386182. The TOI is an NEB, based on LCOGT observations in the PanSTARRS z_s filter showing a depth of roughly 350 ppt. This star was also correctly identified as the host of the signal by the SPOC centroid offset analysis. TRICERATOPS identifies two nearby sources other than the target star bright enough to host the signal, one of which is TIC 250386182. The total NFPP calculated by TRICERATOPS is 0.0311. TIC 250386182 has an NFPP of 0.0311, making it the most probable NFP host. This NFPP is too low to classify the TOI as a likely NFP. However, the calculated FPP of 0.9703 is too high to classify the TOI as a likely planet or validated planet.

5.4. TIC 219388773 (TOI 399.01)

TFOP SG1 confirms that the true host of the signal is TIC 219388775. The TOI is an NEB with depth of 130 ppt, based on LCOGT z_s observations. This star was also correctly

identified as the host of the signal by the SPOC centroid offset analysis. TRICERATOPS identifies one nearby source other than the target star bright enough to host the signal, which is TIC 219388775. The total NFPP calculated by TRICERATOPS is 0.0101. TIC 219388775 has an NFPP of 0.0101, making it the most probable NFP host. This NFPP is too low to classify the TOI as a likely NFP and too high to classify the TOI as a likely planet. In addition, the calculated FPP of 0.2882 is too high to classify the TOI as a validated planet.

5.5. TIC 176778112 (TOI 408.01)

TFOP SG1 confirms that the true host of the signal is TIC 176778114. The TOI is an NEB with primary and secondary eclipse depths of ~ 430 ppt and ~ 300 ppt, respectively, in LCOGT r' observations. This star was also correctly identified as the host of the signal by the SPOC centroid offset analysis. TRICERATOPS identifies two nearby sources other than the target star bright enough to host the signal, one of which is TIC 176778114. The total NFPP calculated by TRICERATOPS is 0.0650. TIC 176778114 has an NFPP of 0.0438, making it the most probable NFP host. This NFPP is too low to classify the TOI as a likely NFP and too high to classify the TOI as a likely planet. In addition, the calculated FPP of 0.3405 is too high to classify the TOI as a validated planet.

5.6. TIC 20178111 (TOI 467.01)

TFOP SG1 confirms that the true host of the signal is TIC 20178112. The TOI is an NEB, based on PEST Observatory R_C observations that show a ~ 55 ppt eclipse on TIC 20178112, which Gaia shows as two stars with magnitudes $G = 14.2$ and $G = 15.9$. This star was also correctly identified as the host of the signal by the SPOC centroid offset analysis. TRICERATOPS identifies three nearby sources other than the target star bright enough to host the signal, one of which is TIC 20178112. The total NFPP calculated by TRICERATOPS is 0.2332. TIC 20178112 has an NFPP of 0.1638, making it the most probable NFP host. This NFPP is high enough to classify the TOI as a likely NFP. In addition, the calculated FPP of 0.4065 is too high to classify the TOI as a validated planet.

5.7. TIC 427352241 (TOI 485.01)

TFOP SG1 confirms that the true host of the signal is TIC 427352247. The TOI is an NEB, based on LCOGT r' observations that show a 200 ppt, V-shaped eclipse. This star was also correctly identified as the host of the signal by the SPOC centroid offset analysis. TRICERATOPS identifies three nearby sources other than the target star bright enough to host the signal, one of which is TIC 427352247. The total NFPP calculated by TRICERATOPS is 0.5219. TIC 427352247 has an NFPP of 0.0693, making it the second most probable NFP host. This NFPP is high enough to classify the TOI as a likely NFP. In addition, the calculated FPP of 0.6498 is too high to classify the TOI as a likely planet or validated planet.

5.8. TIC 108645766 (TOI 497.01)

TFOP SG1 confirms that the true host of the signal is TIC 108645800. The TOI is an NEB, based on LCOGT r' observations with a depth of at least 100 ppt, and confirmed by archival HAT-South data. This star was also correctly identified as the host of the signal by the SPOC centroid offset analysis. TRICERATOPS identifies four nearby sources other than the target star bright enough to host the signal, one of which is TIC 108645800. The total NFPP calculated by TRICERATOPS is 0.6361, but the NFPP around TIC 108645800 was not calculated owing to unknown stellar parameters. This NFPP is high enough to classify the TOI as a likely NFP. In addition, the calculated FPP of 0.8299 is too high to classify the TOI as a likely planet or validated planet.

5.9. TIC 274138511 (TOI 506.01)

TFOP SG1 confirms that the true host of the signal is TIC 760244235. The TOI is an NEB with depth of at least 200 ppt, based on LCOGT r' observations. This star was also correctly identified as the host of the signal by the SPOC centroid offset analysis. TRICERATOPS identifies 10 nearby sources other than the target star bright enough to host the signal, one of which is TIC 760244235. The total NFPP calculated by TRICERATOPS is 0.0507. TIC 760244235 has an NFPP of 0.0030, making it the sixth most probable NFP host. This NFPP is too low to classify the TOI as a likely NFP and too high to classify the TOI as a likely planet. In addition, the calculated FPP of 0.1215 is too high to classify the TOI as a validated planet.

5.10. TIC 431999925 (TOI 513.01)

TFOP SG1 confirms that the true host of the signal is TIC 431999916. The TOI is an NEB with depth of at least 90 ppt, based on LCOGT i' observations. This star was also correctly identified as the host of the signal by the SPOC centroid offset analysis. TRICERATOPS identifies eight nearby sources other than the target star bright enough to host the signal, one of which is TIC 431999916. The total NFPP calculated by TRICERATOPS is 0.9230. TIC 431999916 has an NFPP of 0.1482, making it the second most probable NFP host. This NFPP is high enough to classify the TOI as a likely NFP. In addition, the calculated FPP of 0.9819 is too high to classify the TOI as a likely planet or validated planet.

5.11. TIC 438490744 (TOI 529.01)

TFOP SG1 confirms that the true host of the signal is TIC 438490748. The TOI is an NEB with depth of ~ 80 ppt, based on K2 and HAT-South data. TIC 438490748 (the source of the signal) is a pair of stars in Gaia, so the true depth may be deeper. This star was also correctly identified as the host of the signal by the SPOC centroid offset analysis. TRICERATOPS identifies two nearby sources other than the target star bright enough to host the signal, one of which is TIC 438490748. The total NFPP calculated by TRICERATOPS is 0.9938. TIC 438490748 has an NFPP of 0.9938, making it the most probable NFP host. This NFPP is high enough to classify the TOI as a likely NFP. In addition, the calculated FPP of 1.0 is too high to classify the TOI as a likely planet or validated planet.

5.12. TIC 302895996 (TOI 531.01)

TFOP SG1 confirms that the true host of the signal is TIC 302895984. The TOI is an NEB with a depth of 200 ppt in the I band from LCOGT observations. This star was also correctly identified as the host of the signal by the SPOC centroid offset analysis. TRICERATOPS identifies five nearby sources other than the target star bright enough to host the signal, one of which is TIC 302895984. The total NFPP calculated by TRICERATOPS is 0.7971. TIC 302895984 has an NFPP of 0.0509, making it the third most probable NFP host. This NFPP is high enough to classify the TOI as a likely NFP. In addition, the calculated FPP of 0.9477 is too high to classify the TOI as a likely planet or validated planet.

5.13. TIC 53593457 (TOI 543.01)

TFOP SG1 confirms that the true host of the signal is TIC 53593470. The TOI is an NEB with a depth of ~ 250 ppt in both g' and i' in LCOGT observations. This star was also correctly identified as the host of the signal by the SPOC centroid offset analysis. TRICERATOPS identifies five nearby sources other than the target star bright enough to host the signal, one of which is TIC 53593470. The total NFPP calculated by TRICERATOPS is 0.6436, but the NFPP around TIC 53593470 was not calculated owing to unknown stellar parameters. This NFPP is high enough to classify the TOI as a likely NFP. In addition, the calculated FPP of 0.9580 is too high to classify the TOI as a likely planet or validated planet.

5.14. TIC 59003115 (TOI 556.01)

TFOP SG1 confirms that the true host of the signal is TIC 59003118. This is K2-78b (EPIC 210400751; Crossfield et al. 2016), which was later shown to be an NEB (Cabrera et al. 2017). This star was also correctly identified as the host of the signal by the SPOC centroid offset analysis. TRICERATOPS identifies two nearby sources other than the target star bright enough to host the signal, one of which is TIC 59003118. The total NFPP calculated by TRICERATOPS is 0.0258. TIC 59003118 has an NFPP of 0.0050, making it the second most probable NFP host. This NFPP is too low to classify the TOI as a likely NFP and too high to classify the TOI as a likely planet. In addition, the calculated FPP of 0.2854 is too high to classify the TOI as a validated planet.

5.15. TIC 1133072 (TOI 566.01)

TFOP SG1 confirms that the true host of the signal is TIC 830310300. The TOI is an NEB, based on observations from LCOGT and Mt. Kent Observatory in i' and from El Sauce Observatory in R_C . The depth is at least 500 ppt in i' . In this case, the SPOC centroid offset analysis failed to identify the presence of a background source at the 3σ level of significance. TRICERATOPS identifies nine nearby sources other than the target star bright enough to host the signal, one of which is TIC 830310300. The total NFPP calculated by TRICERATOPS is 0.8854. TIC 830310300 has an NFPP of 0.0124, making it the sixth most probable NFP host. This NFPP is high enough to classify the TOI as a likely NFP. In addition, the calculated FPP of 0.9687 is too high to classify the TOI as a likely planet or validated planet.

5.16. TIC 146463781 (TOI 636.01)

TFOP SG1 confirms that the true host of the signal is TIC 146463868. The TOI is an NEB, based on LCOGT I_C -band observations with a depth of 300 ppt. This star was also correctly identified as the host of the signal by the SPOC centroid offset analysis. TRICERATOPS identifies three nearby sources other than the target star bright enough to host the signal, one of which is TIC 146463868. The total NFPP calculated by TRICERATOPS is 0.8640, but the NFPP around TIC 146463868 was not calculated owing to unknown stellar parameters. This NFPP is high enough to classify the TOI as a likely NFP. In addition, the calculated FPP of 0.9887 is too high to classify the TOI as a likely planet or validated planet.

5.17. TIC 432008938 (TOI 643.01)

TFOP SG1 confirms that the true host of the signal is TIC 432008934. The TOI is an NEB, based on the centroid offset from the SPOC S01–S09 vetting report. TRICERATOPS identifies two nearby sources other than the target star bright enough to host the signal, but neither is TIC 432008934. The total NFPP calculated by TRICERATOPS is $1e - 5$. This NFPP is too low to classify the TOI as a likely NFP. However, the calculated FPP of 0.9996 is too high to classify the TOI as a likely planet or validated planet.

5.18. TIC 54085154 (TOI 662.01)

TFOP SG1 confirms that the true host of the signal is TIC 54085149. The TOI is an NEB, based on LCOGT i' observations that show a depth of 400 ppt at two different epochs. In this case, the SPOC centroid offset analysis found a significant offset, but the offset did not point directly to the true host. TRICERATOPS identifies two nearby sources other than the target star bright enough to host the signal, one of which is TIC 54085149. The total NFPP calculated by TRICERATOPS is 0.0013. TIC 54085149 has an NFPP of 0.0008, making it the most probable NFP host. This NFPP is too low to classify the TOI as a likely NFP and too high to classify the TOI as a likely planet. In addition, the calculated FPP of 0.2747 is too high to classify the TOI as a validated planet.

5.19. TIC 147660201 (TOI 670.01)

TFOP SG1 confirms that the true host of the signal is TIC 147660207. This candidate was retired from SG1 as a nearby planet candidate. Observations show the true source of the

signal to be a ~ 4 ppt event in the nearby star TIC 147660207, which is still an active planet candidate as of this writing. The event was seen in R_C from El Sauce Observatory and in i' from Mt. Kent and Hazelwood Observatories. This star was also correctly identified as the host of the signal by the SPOC centroid offset analysis. TRICERATOPS identifies nine nearby sources other than the target star bright enough to host the signal, one of which is TIC 147660207. The total NFPP calculated by TRICERATOPS is 0.1652. TIC 147660207 has an NFPP of 0.0868, making it the most probable NFP host. This NFPP is high enough to classify the TOI as a likely NFP. In addition, the calculated FPP of 0.6543 is too high to classify the TOI as a likely planet or validated planet.

5.20. TIC 391821647 (TOI 708.01)

TFOP SG1 confirms that the TOI is an NFP. The TOI is an NEB, based on large scatter in the image centroid from sector to sector in a very crowded field and a possible secondary eclipse. From the SPOC S01–S09 report, this is a clear NEB $\sim 35''$ west. Although the exact source of the NEB is not clear from the SPOC centroid offset analysis, it is likely too faint, and thus the event is too deep to be planetary. TRICERATOPS identifies 141 nearby sources other than the target star bright enough to host the signal. The total NFPP calculated by TRICERATOPS is 0.1760. This NFPP is high enough to classify the TOI as a likely NFP. In addition, the calculated FPP of 0.5955 is too high to classify the TOI as a likely planet or validated planet.

5.21. TIC 373424049 (TOI 742.01)

TFOP SG1 confirms that the true host of the signal is TIC 373424060. The TOI is an NEB, based on LCOGT observations that show a depth of ~ 200 ppt in the z_s filter. This star was also correctly identified as the host of the signal by the SPOC centroid offset analysis. TRICERATOPS identifies 31 nearby sources other than the target star bright enough to host the signal, one of which is TIC 373424060. The total NFPP calculated by TRICERATOPS is 0.2268. TIC 373424060 has an NFPP of 0.0006, making it the 23rd most probable NFP host. This NFPP is high enough to classify the TOI as a likely NFP. In addition, the calculated FPP of 0.4377 is too high to classify the TOI as a validated planet.

5.22. TIC 271596418 (TOI 868.01)

TFOP SG1 confirms that the true host of the signal is TIC 271596416. The TOI is an NEB, based on LCOGT observations that show a depth of 70–100 ppt in z_s and ~ 30 ppt in i' . This star was also correctly identified as the host of the signal by the SPOC centroid offset analysis. TRICERATOPS identifies seven nearby sources other than the target star bright enough to host the signal, one of which is TIC 271596416. The total NFPP calculated by TRICERATOPS is 0.0259. TIC 271596416 has an NFPP of 0.0078, making it the most probable NFP host. This NFPP is too low to classify the TOI as a likely NFP and too high to classify the TOI as a likely planet. In addition, the calculated FPP of 0.6551 is too high to classify the TOI as a validated planet.

5.23. TIC 364107753 (TOI 909.01)

TFOP SG1 confirms that the true host of the signal is TIC 1310226289. The TOI is an NEB, based on LCOGT observations that show a depth of at least 75 ppt in z_s . This star was also correctly identified as the host of the signal by the SPOC centroid offset analysis. TRICERATOPS identifies four nearby sources other than the target star bright enough to host the signal, one of which is TIC 1310226289. The total NFPP calculated by TRICERATOPS is 0.0131. TIC 1310226289 has an NFPP of 0.0068, making it the most probable NFP host. This NFPP is too low to classify the TOI as a likely NFP and too high to classify the TOI as a likely planet. In addition, the calculated FPP of 0.0645 is too high to classify the TOI as a validated planet.

5.24. TIC 253990973 (TOI 1061.01)

TFOP SG1 confirms that the true host of the signal is TIC 253985122. The TOI is an NEB, based on PEST Observatory R_C -band observations with a depth of ~ 600 ppt. In this case, the SPOC centroid offset analysis failed to identify the presence of a background source at the 3σ level of significance. TRICERATOPS identifies nine nearby sources other than the target star bright enough to host the signal, one of which is TIC 253985122. The total NFPP calculated by TRICERATOPS is 0.0315. TIC 253985122 has an NFPP of 0.0037, making it the fourth most probable NFP host. This NFPP is too low to classify the TOI as a likely NFP and too high to classify the TOI as a likely planet. In addition, the calculated FPP of 0.5030 is too high to classify the TOI as a likely planet or validated planet.

5.25. TIC 308034948 (TOI 1206.01)

TFOP SG1 confirms that the TOI is an NEB. Stellar parameters from Gaia and TIC indicate $R_* > 40R_\odot$, but the orbital period of < 1 day would place the companion's orbit inside the star if it were on target. The SPOC centroid offset suggests that the signal originates from a star to the south. TRICERATOPS identifies 108 nearby sources other than the target star bright enough to host the signal. The total NFPP calculated by TRICERATOPS is 0.0383. This NFPP is too low to classify the TOI as a likely NFP and too high to classify the TOI as a likely planet. In addition, the calculated FPP of 0.7727 is too high to classify the TOI as a likely planet or validated planet.

5.26. TIC 274762761 (TOI 1256.01)

TFOP SG1 confirms that the true host of the signal is TIC 274762865. The TOI is an NEB, based on archival MEarth-North (Nutzman & Charbonneau 2008; Irwin et al. 2015) observations that show no event on target and eclipses at the TESS ephemeris in a neighboring star. SPOC difference image analysis correctly identified this star as the true host. TRICERATOPS identifies six nearby sources other than the target star bright enough to host the signal, one of which is TIC 274762865. The total NFPP calculated by TRICERATOPS is 0.9869, but the NFPP around TIC 274762865 was not calculated owing to unknown stellar parameters. This NFPP is high enough to classify the TOI as a likely NFP. In addition, the calculated FPP of 0.9981 is too high to classify the TOI as a likely planet or validated planet.

5.27. TIC 267561446 (TOI 1284.01)

TFOP SG1 confirms that the true host of the signal is TIC 267561450. The TOI is an NEB, based on observations by the University of Louisville Manner Telescope and MuSCAT2 at Teide Observatory in g' , r' , i' , and z' that show a ~ 200 ppt eclipse. This star was also correctly identified as the host of the signal by the SPOC centroid offset analysis. TRICERATOPS identifies 13 nearby sources other than the target star bright enough to host the signal, one of which is TIC 267561450. The total NFPP calculated by TRICERATOPS is 0.2818. TIC 267561450 has an NFPP of 0.0235, making it the fourth most probable NFP host. This NFPP is high enough to classify the TOI as a likely NFP. In addition, the calculated FPP of 0.7151 is too high to classify the TOI as a likely planet or validated planet.

5.28. TIC 274662200 (TOI 1285.01)

TFOP SG1 confirms that the true host of the signal is TIC 274662220. The TOI is an NEB, based on observations at the University of Louisville Manner Telescope that show a depth of 150 ppt in r' . This star was also correctly identified as the host of the signal by the SPOC centroid offset analysis. TRICERATOPS identifies 21 nearby sources other than the target star bright enough to host the signal, one of which is TIC 274662220. The total NFPP calculated by TRICERATOPS is 0.3031. TIC 274662220 has an NFPP of 0.0501, making it the second most probable NFP host. This NFPP is high enough to classify the TOI as a likely NFP. In addition, the calculated FPP of 0.6880 is too high to classify the TOI as a likely planet or validated planet.

5.29. TIC 408203470 (TOI 1289.01)

TFOP SG1 confirms that the true host of the signal is TIC 408203452. The TOI is an NEB, based on observations in a long-pass GG495 filter at the Steward Observatory Phillips 0.6 m Telescope on Mount Lemmon that show a 35 ppt eclipse. Observations at the University of Louisville Moore Observatory show a depth of 60 ppt in r' . This star was also correctly identified as the host of the signal by the SPOC centroid offset analysis. TRICERATOPS identifies 10 nearby sources other than the target star bright enough to host the signal, one of which is TIC 408203452. The total NFPP calculated by TRICERATOPS is 0.3258. TIC 408203452 has an NFPP of 0.1435, making it the most probable NFP host. This NFPP is high enough to classify the TOI as a likely NFP. In addition, the calculated FPP of 0.8512 is too high to classify the TOI as a likely planet or validated planet.

5.30. TIC 233681149 (TOI 1340.01)

TFOP SG1 confirms that the true host of the signal is TIC 233681148. The TOI is an NEB, based on SPOC S14-S16 reports that show a centroid offset to the closest star SW. Single-pixel photometry on the TESS FFIs supports this conclusion. TRICERATOPS identifies one nearby source other than the target star bright enough to host the signal, which is TIC 233681148. The total NFPP calculated by TRICERATOPS is 0.0309. TIC 233681148 has an NFPP of 0.0309, making it the most probable NFP host. This NFPP is too low to classify the TOI as a likely NFP and too high to classify the TOI as a likely planet. In addition, the calculated FPP of 0.0947 is too high to classify the TOI as a validated planet.

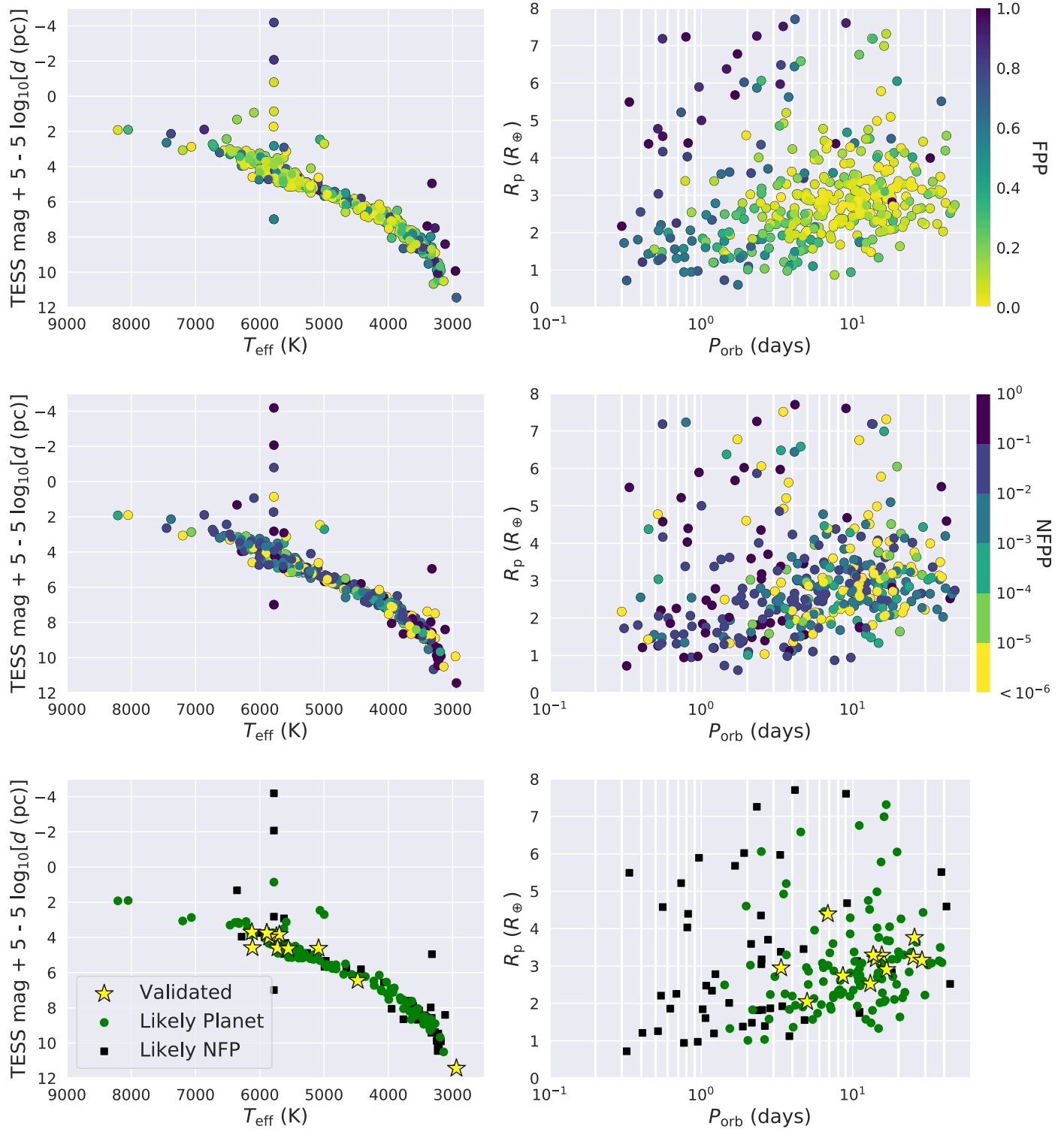


Figure 16. Host star properties (left) and planet properties (right) of analyzed TOI systems. In the top panels, we color each system according to its FPP. In the middle panels, we color each system according to its NFPP. In the bottom panels, we distinguish TOIs that have been classified as validated planets, likely planets, and likely NFPs. In general, planets with smaller radii and longer orbital periods are more likely to be identified as planets. The vertical stack of stars at $T_{\text{eff}} \sim 6000$ K are stars with unknown surface temperatures that were assigned a solar T_{eff} on the TFOF website.

6. Results

We apply our code to 384 SPOC TOIs that have neither been confirmed as bona fide planets nor rejected as false positives by TFOF. We again restrict our analysis to TOIs with $R_p < 8R_{\oplus}$, TOIs with host stars that are well characterized in the TIC, and

TOIs for which we are able to recover a transit with the purported orbital parameters. However, unlike the sample used in Section 4, we permit TOIs with orbital periods up to 50 days and extract their light curves using data from all sectors in which they were observed. The results of these calculations are displayed in Figure 16.

Table 6
Statistically Validated TOIs

TOI Number	FPP	Original Validation Paper
261.01	0.0067 ± 0.0004	This work
261.02	0.0009 ± 0.0002	This work
469.01	0.0133 ± 0.0016	This work
682.01	0.0069 ± 0.0020	This work
736.01	0.0092 ± 0.0005	Crossfield et al. (2019)
836.01	0.0141 ± 0.0019	This work
1054.01	0.0115 ± 0.0008	This work
1203.01	0.0125 ± 0.0011	This work
1230.01	0.0132 ± 0.0005	This work
1233.01	0.0135 ± 0.0012	Daylan et al. (2020)
1339.02	0.0127 ± 0.0011	Badenas-Agusti et al. (2020)
1774.01	0.0133 ± 0.0010	This work

In the top panels of Figure 16, we show the host star and planet properties of all TOIs color-coded by FPP. In these panels, we see that TOIs with smaller radii and longer orbital periods tend to have lower FPPs. In the middle panels of the figure, we show the same data color-coded by NFPP. In these panels, we again see a propensity for TOIs with smaller radii and longer orbital periods to have lower NFPPs. Nonetheless, there are several TOIs with large radii and short orbital periods that have low NFPP values, which generally represent TOIs without nearby stars bright enough to produce their observed transits. Additionally, we see that neither FPP nor NFPP is closely tied to host spectral type.

In the bottom panels of Figure 16, we present the properties of TOIs that have been classified as validated planets, likely planets, and likely NFPs by our analysis. In total, we statistically validate 12 TOIs, identify 125 TOIs as likely planets, and identify 52 likely NFPs. Our sample of validated TOIs have host stars with a variety of spectral types and planets with radii ranging from $1R_{\oplus}$ to $5R_{\oplus}$ and orbital periods ranging from 3 to 30 days. The details for all tested TOIs are given in Table 7.

The TOI numbers of the planet candidates statistically validated in this analysis are presented in Table 6. Of these, nine are newly validated and three have already been empirically validated via a combination of follow-up observations. The agreement of our statistical validation and the empirical validation of these planet candidates is encouraging for the efficacy of both methods. In addition, we include the FPP calculated by TRICERATOPS in Table 6. Because FPP is expected to have some scatter across runs, we perform the calculation 20 times for each validated TOI and list the mean and standard deviation of the resulting distribution. In doing so, we affirm that our original FPP calculation that validated the planet candidate was not an outlier.

7. Discussion

In Figure 16 we present the results of TRICERATOPS runs for 384 TOIs, 189 of which are assigned classifications of validated planet, likely planet, or likely NFP. These results are also shown in Table 7, which is available in its entirety in machine-readable format. In these results, a number of patterns emerge that could have broader implications for the population of planets detected by TESS and the TESS FP rate. As we noted previously, TOIs classified as validated planets or likely planets generally have smaller radii and longer orbital periods.

One could interpret this as meaning that planets are more common in this region of parameter space. However, we would be remiss if we did not acknowledge that this result is in part due to our choice of R_p and P_{orb} priors, which prefer transiting planet scenarios in this region of parameter space. We realize that this effect could be concerning for those who wish to use TRICERATOPS for large-scale statistical studies of planets detected by TESS, especially in the case where the true underlying prior distributions are unknown, because it could bias their results to agree with previous planet occurrence rate studies. We therefore plan to add alternative prior distributions, such as a uniform prior, that the user can select when they wish their results to be free of such a bias.

To test the extent to which our results are biased by our prior distribution for R_p , we reran our code on all 384 TOIs with a uniform R_p prior. Because our original R_p prior penalizes planet candidates with $R_p > 5R_{\oplus}$, one might expect more of these planet candidates to be classified as validated planets or likely planets when the uniform prior is applied. With the uniform prior, the number of validated planets decreased from 12 to 2 (the number of which with $R_p > 5R_{\oplus}$ increased from 0 to 1), the number of likely planets decreased from 125 to 93 (the number of which with $R_p > 5R_{\oplus}$ increased from 8 to 9), and the number of likely NFPs increased from 52 to 93 (the number of which with $R_p > 5R_{\oplus}$ did not change). These results show that the chance of a planet candidate being classified as a validated planet or a likely NFP is strongly dependent on the choice of R_p prior. However, as we do not see a large change in the number of classifications for TOIs with $R_p > 5R_{\oplus}$, we cannot conclude that our original R_p prior significantly biases our results against these TOIs.

Another notable feature of Figure 16 is the large number of ultra-short-period planet (i.e., planets with $P_{\text{orb}} < 1$ day) TOIs, of which there are 41 with $R_p < 8R_{\oplus}$. Past studies have found that this type of planet only occurs around $<1\%$ of stars (Sanchis-Ojeda et al. 2014; Adams et al. 2016), but the true rate could be higher if all of these candidates are actual planets. However, this interpretation is dependent on the actual false-positive rate of these TOIs. The fact that TRICERATOPS classifies none of these USP candidates as likely planets and many as NFPs suggests that this false-positive rate is high. To ensure that this prediction is not an artifact of the aforementioned P_{orb} prior (which is biased toward eclipsing binary scenarios in this region of parameter space), we also repeated our calculations without this prior. Upon removing the prior, the number of likely planets increased from 125 to 127, while the number of validated planets and likely NFPs remained the same. The increase can be attributed to three ultra-short-period planet candidates (TOIs 460.01, 561.02, and 864.01) whose classifications were changed from likely NFP to likely planet. This small increase in the number of likely planets suggests that our results are only moderately affected by our P_{orb} prior, and that most ultra-short-period planet candidates are in fact false positives.

In addition to a statistical validation tool, TRICERATOPS can be used as a vetting tool to prioritize follow-up observations of TOIs. Consider candidates that are classified as likely planets, but with FPPs just above the validation threshold. Several TOIs we classify as likely planets match this description, and some (e.g., TOI 1055; Bedell et al., in preparation) have been confirmed concurrently with this paper. These TOIs make would ideal targets for high-resolution

Table 7
TRICERATOPS Predictions for Undesignated TOIs

TIC ID	TOI Number	R_p (R_{\oplus})	P_{orb} (days)	S/N	FPP	NFPP	# NFP Candidates	Classification
278683844	119.01	2.13	5.54	8.3	0.04	9.25e-05	2	Likely planet
278683844	119.02	1.93	10.69	7.0	0.06	1.88e-04	2	Likely planet
231702397	122.01	2.51	5.08	6.6	0.06	2.79e-05	1	Likely planet
52368076	125.03	3.38	19.98	4.0	0.04	0.00e+00	0	Likely planet
391949880	128.01	3.06	4.94	6.9	0.10	2.76e-02	4	
263003176	130.01	2.32	14.34	4.3	0.04	4.02e-03	2	
89020549	132.01	3.02	2.11	12.4	0.03	8.12e-05	1	Likely planet
219338557	133.01	2.37	8.20	10.5	0.05	0.00e+00	1	Likely planet
234994474	134.01	1.49	1.40	17.3	0.11	7.62e-03	4	
62483237	139.01	2.93	11.06	13.0	0.03	0.00e+00	0	Likely planet

Note. This table is published in its entirety in machine-readable format.

(This table is available in its entirety in machine-readable form.)

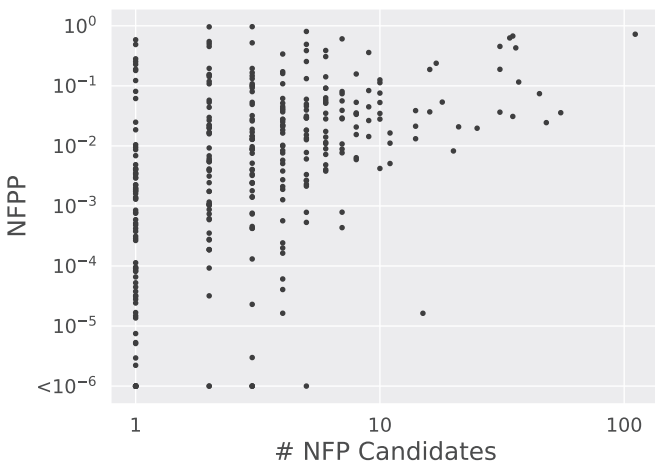


Figure 17. NFPP vs. number of nearby stars bright enough to be an NFP for each of the 384 TOIs tested in Section 6. TOIs with no potential NFPs are omitted. While the average NFPP increases as the number of possible NFPs increases, TRICERATOPS is able to classify TOIs with any number of nearby host candidates as likely NFPs ($\text{NFPP} > 10^{-1}$).

imaging follow-up, because the resulting data products can be incorporated to achieve a lower FPP and validate the planet candidate. In addition, we displayed in Section 5 that TRICERATOPS is proficient at identifying NFPs and is often able to predict which nearby star hosts the observed signal. By prioritizing nearby stars with high probabilities of hosting NFPs, observers can increase the rate of true NFP identification. Doing so would allow other members of the TESS follow-up community to focus on TOIs that are more likely to be bona fide planets. To display the broad applicability of this prioritization method (i.e., to show that it is not only relevant for TOIs in very crowded fields), we show in Figure 17 the NFPP as a function of the number of nearby stars bright enough to be NFPs for the 384 TOIs in our analysis. As one might predict, the expected NFPP increases in more crowded fields. Nonetheless, TOIs with as few as one NFP candidate can be classified as likely NFPs. In other words, TRICERATOPS provides information pertaining to the probability of a given TOI being an NFP beyond what can be gathered from the crowdedness of the surrounding field.

Our tool can also be combined with other validation and vetting tools to provide even more robust validation analyses.

As of now, TRICERATOPS is the only validation tool compatible with TESS data that models transits from nearby contaminant stars. Seeing as identifying NFPs is one of the strengths of our tool, it can be used as the first step in such an analysis. For example, one could use TRICERATOPS to identify TOIs with sufficiently low NFPPs and then use tools like VESPA (Morton 2012, 2015) and DAVE (Kostov et al. 2019) to further constrain the FPP of the planet candidate around the target star. Additionally, comparing the results of several tools would allow one to build a stronger statistical argument for or against the existence of a planet.

To improve the utility of TRICERATOPS, we plan on adding features that will make the procedure more efficient and robust. First, we will add a feature that searches for in-transit centroid offsets to constrain the probabilities of NFPs. Second, we will improve our priors by expanding to more dimensions that affect planet occurrence rates, such as planet multiplicity. In this vein, it has been shown that planet candidates that are members of systems with multiple planet candidates are almost always bona fide planets (e.g., Lissauer et al. 2012). This in and of itself is strong evidence that candidate multiplanet systems with validated planets (including TOIs 736, 836, 1233, and 1339) actually host multiple transiting planets. Third, we will make our tool compatible with additional follow-up constraints, such as time-series photometry that rules out signals around nearby stars and spectroscopic observations that provide limits on eclipsing binary properties, to improve its ability to validate planet candidates. Lastly, we will add additional astrophysical scenarios to our calculation procedure, such as that involving a noncircular orbit and that involving an eclipsing binary where only the secondary eclipse is detected.

8. Conclusions

We present a new tool, TRICERATOPS, designed for rapid validation of TESS Objects of Interest. Using a Bayesian framework, this tool calculates the probabilities of various transit-producing scenarios for a given TOI in order to provide an FPP and an NFPP. Our tool is also able to fold in information from follow-up observations as additional constraints in these calculations.

We test our tool on 68 TOIs that have been designated as either confirmed planets or astrophysical false positives by members of the TESS Observation Follow-up Program (TFOP) based on follow-up observations. We define three

classifications based on the results of this analysis. For a TOI to be validated, it must have short-cadence observations, $\text{NFPP} < 10^{-3}$, and $\text{FPP} < 0.015$. For a TOI to be classified as a likely planet, it must have $\text{NFPP} < 10^{-3}$ and $\text{FPP} < 0.5$. Lastly, for a TOI to be classified as a likely NFP, it must have $\text{NFPP} > 10^{-1}$. To display the proficiency of our tool in identifying NFPs, we also compare our predictions to TOIs that have been identified as actual NFPs by TFOP.

We apply our tool to 384 TOIs with 2-minute cadence observations that have not yet been classified as confirmed planets or rejected as false positives. We statistically validate 12 TOIs, classify 125 TOIs as likely planets, and classify 52 TOIs as likely NFPs.

In addition to planet validation, we recommend using TRICERATOPS to identify TOIs with high probabilities of being planets or NFPs and prioritizing these candidates as targets for further vetting via follow-up observations. When used in combination with other vetting tools, such as VESPA and DAVE, our tool can also be utilized to perform even more thorough validation analyses of planet candidates. We hope this tool will be a valuable resource in the search for planets with TESS.

We thank the referee Timothy D. Morton (the creator of the VESPA analysis) for his careful analysis and review, in response to which both the TRICERATOPS analysis and this paper have been significantly improved. We thank Stephen T. Bryson, Jack J. Lissauer, Rachel B. Fernandes, Ellianna Schwab Abrahams, Arjun B. Savel, and David W. Latham for helpful conversations and guidance that improved this paper. We thank Jonathan M. Irwin for the collection and contribution of MEarth data used in this paper. We also thank the TESS follow-up community for making this work possible through their efforts to vet planet candidates.

We thank the NASA TESS Guest Investigator Program for supporting this work through grant 80NSSC18K1583 (awarded to C.D.D.). S.G. and C.D.D. also appreciate and acknowledge support from the Hellman Fellows Fund, the Alfred P. Sloan Foundation, the David and Lucile Packard Foundation, and the NASA Exoplanets Research Program (XRP) through grant 80NSSC20K0250.










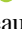












This work makes use of observations from the LCOGT network. This material is based on work supported by the National Science Foundation Graduate Research Fellowship Program under grant No. DGE-1650115. The research leading to these results has received funding from the ARC grant for Concerted Research Actions, financed by the Wallonia-Brussels Federation. TRAPPIST is funded by the Belgian Fund for Scientific Research (Fond National de la Recherche Scientifique, FNRS) under the grant FRFC 2.5.594.09.F, with the participation of the Swiss National Science Foundation (SNF). M.G. and E.J. are F.R.S.-FNRS Senior Research Associates. The MEarth Team gratefully acknowledges the David and Lucile Packard Fellowship for Science and Engineering (awarded to D.C.), continued support by the NSF mostly recently under grant AST-1616624, and support by NASA under grant 80NSSC18K0476 (XRP Program). This work is made possible by a grant from the John Templeton Foundation. The opinions expressed in this publication are those of the authors and do not necessarily reflect the views of the John Templeton Foundation. J.N.W. thanks the Heising-Simons Foundation for support.

Funding for the TESS mission is provided by NASA's Science Mission directorate. This research has made use of the Exoplanet Follow-up Observation Program website, which is operated by the California Institute of Technology, under contract with the National Aeronautics and Space Administration under the Exoplanet Exploration Program. This paper includes data collected by the TESS mission, which are publicly available from the Mikulski Archive for Space Telescopes (MAST). We acknowledge the use of public TESS Alert data from pipelines at the TESS Science Office and TESS Science Processing Operations Center. Resources supporting this work were provided by the NASA High-End Computing (HEC) Program through the NASA Advanced Supercomputing (NAS) Division at Ames Research Center for the production of the SPOC data products.

Facilities: TESS, Shane Telescope, CDK20N, Univ. Louisville 0.6m Telescope, LCOGT, Fred Lawrence Whipple Observatory, Carlos Sanchez Infrared Telescope, PEST, HATNet, TRAPPIST, Steward Observatory Phillips Telescope.

Software: NumPy (Oliphant 2006), SciPy (Virtanen et al. 2019), pandas (McKinney 2011) matplotlib (Hunter 2007), astropy (Price-Whelan et al. 2018), batman (Kreidberg 2015), lightkurve (Lightkurve Collaboration et al. 2018), eleanor (Feinstein et al. 2019), VESPA (Morton 2012, 2015).

ORCID iDs

Steven Giacalone  <https://orcid.org/0000-0002-8965-3969>
 Courtney D. Dressing  <https://orcid.org/0000-0001-8189-0233>
 Eric L. N. Jensen  <https://orcid.org/0000-0002-4625-7333>
 Karen A. Collins  <https://orcid.org/0000-0001-6588-9574>
 George R. Ricker  <https://orcid.org/0000-0003-2058-6662>
 Roland Vanderspek  <https://orcid.org/0000-0001-6763-6562>
 S. Seager  <https://orcid.org/0000-0002-6892-6948>
 Joshua N. Winn  <https://orcid.org/0000-0002-4265-047X>
 Jon M. Jenkins  <https://orcid.org/0000-0002-4715-9460>
 Thomas Barclay  <https://orcid.org/0000-0001-7139-2724>
 Khalid Barkaoui  <https://orcid.org/0000-0003-1464-9276>
 Charles Cadieux  <https://orcid.org/0000-0001-9291-5555>
 David Charbonneau  <https://orcid.org/0000-0002-9003-484X>
 Kevin I. Collins  <https://orcid.org/0000-0003-2781-3207>
 Dennis M. Conti  <https://orcid.org/0000-0003-2239-0567>
 René Doyon  <https://orcid.org/0000-0001-5485-4675>
 Phil Evans  <https://orcid.org/0000-0002-5674-2404>
 Michaël Gillon  <https://orcid.org/0000-0003-1462-7739>
 Natalia M. Guerrero  <https://orcid.org/0000-0002-5169-9427>
 Emmanuël Jehin  <https://orcid.org/0000-0001-8923-488X>
 John F. Kielkopf  <https://orcid.org/0000-0003-0497-2651>
 Brian McLean  <https://orcid.org/0000-0002-8058-643X>
 Enric Palle  <https://orcid.org/0000-0003-0987-1593>
 Hannu Parviainen  <https://orcid.org/0000-0001-5519-1391>
 Francisco J. Pozuelos  <https://orcid.org/0000-0003-1572-7707>
 Avi Shporer  <https://orcid.org/0000-0002-1836-3120>
 Quentin Socia  <https://orcid.org/0000-0002-7434-0863>
 Chris Stockdale  <https://orcid.org/0000-0003-2163-1437>
 Thiam-Guan Tan  <https://orcid.org/0000-0001-5603-6895>
 Guillermo Torres  <https://orcid.org/0000-0002-5286-0251>
 Joseph D. Twicken  <https://orcid.org/0000-0002-6778-7552>

William C. Waalkes  <https://orcid.org/0000-0002-8961-0352>

Ian A. Waite  <https://orcid.org/0000-0002-3249-3538>

References

- Adams, E. R., Jackson, B., & Endl, M. 2016, *AJ*, **152**, 47
- Alonso, R., Brown, T. M., Torres, G., et al. 2004, *ApJL*, **613**, L153
- Ansdell, M., Ioannou, Y., Osborn, H. P., et al. 2018, *ApJL*, **869**, L7
- Badenas-Agusti, M., Günther, M. N., Daylan, T., et al. 2020, *AJ*, **160**, 113
- Brown, A., Vallenari, A., Prusti, T., et al. 2018, *A&A*, **616**, A1
- Brown, T. M., Baliber, N., Bianco, F. B., et al. 2013, *PASP*, **125**, 1031
- Bryson, S. T., Jenkins, J. M., Gilliland, R. L., et al. 2013, *PASP*, **125**, 889
- Burke, C. J., Christiansen, J. L., Mullally, F., et al. 2015, *ApJ*, **809**, 8
- Cabrera, J., Barros, S. C. C., Armstrong, D., et al. 2017, *A&A*, **606**, A75
- Catanzarite, J. H. 2015, *Autovetter Planet Candidate Catalog for Q1-Q17 Data Release 24*, Tech. Rep. KSCI-19091-001, <https://exoplanetarchive.ipac.caltech.edu/docs/KSCI-19091>
- Christiansen, J. L., Jenkins, J. M., Caldwell, D. A., et al. 2012, *PASP*, **124**, 1279
- Claret, A. 2018, *A&A*, **618**, A20
- Cloutier, R. 2019, *AJ*, **158**, 81
- Cloutier, R., Rodriguez, J. E., Irwin, J., et al. 2020, *AJ*, **160**, 22
- Coughlin, J. L., Thompson, S. E., Bryson, S. T., et al. 2014, *AJ*, **147**, 119
- Crossfield, I. J., Ciardi, D. R., Petigura, E. A., et al. 2016, *ApJS*, **226**, 7
- Crossfield, I. J., Waalkes, W., Newton, E. R., et al. 2019, *ApJL*, **883**, L16
- Daylan, T., Pingle, K., Wright, J., et al. 2020, *arXiv:2004.11314*
- Demangeon, O. D., Faedi, F., Hébrard, G., et al. 2018, *A&A*, **610**, A63
- Díaz, R. F., Almenara, J. M., Santerne, A., et al. 2014, *MNRAS*, **441**, 983
- Dong, S., & Zhu, Z. 2013, *ApJ*, **778**, 53
- Dressing, C. D., & Charbonneau, D. 2013, *ApJ*, **767**, 95
- Dressing, C. D., & Charbonneau, D. 2015, *ApJ*, **807**, 45
- Eisner, N., Barragán, O., Aigrain, S., et al. 2020, *MNRAS*, **494**, 750
- Ermann, R., Torres, G., Schmidt, T. O., et al. 2014, *AN*, **335**, 345
- Feinstein, A. D., Montet, B. T., Foreman-Mackey, D., et al. 2019, *PASP*, **131**, 094502
- Foreman-Mackey, D., Hogg, D. W., & Morton, T. D. 2014, *ApJ*, **795**, 64
- Fressin, F., Torres, G., Charbonneau, D., et al. 2013, *ApJ*, **766**, 81
- Fulton, B. J., Petigura, E. A., Howard, A. W., et al. 2017, *AJ*, **154**, 109
- Giacalone, S., Matsakos, T., & Königl, A. 2017, *AJ*, **154**, 192
- Gilbert, E. A., Barclay, T., Schlieder, J. E., et al. 2020, *AJ*, **160**, 116
- Ginsburg, A., Sipőcz, B. M., Brasseur, C., et al. 2019, *AJ*, **157**, 98
- Girardi, L., Groenewegen, M., Hatziminaoglou, E., & Da Costa, L. 2005, *A&A*, **436**, 895
- Günther, M. N., Pozuelos, F. J., Dittmann, J. A., et al. 2019, *NatAs*, **3**, 1099
- Hirsch, L. A., Ciardi, D. R., Howard, A. W., et al. 2019, *ApJ*, **878**, 50
- Howard, A. W., Marcy, G. W., Bryson, S. T., et al. 2012, *ApJS*, **201**, 15
- Hsu, D. C., Ford, E. B., Ragozzine, D., & Morehead, R. C. 2018, *AJ*, **155**, 205
- Huang, C. X., Quinn, S. N., Vanderburg, A., et al. 2020, *ApJL*, **892**, L7
- Hunter, J. D. 2007, *CSE*, **9**, 90
- Irwin, J. M., Berta-Thompson, Z. K., Charbonneau, D., et al. 2015, in *18th Cambridge Workshop on Cool Stars, Stellar Systems, and the Sun*, ed. G. van Belle & H. C. Harris (Flagstaff, AZ: Lowell Observatory), 767
- Jenkins, J. M., Twicken, J. D., McCauliff, S., et al. 2016, *Proc. SPIE*, **9913**, 99133E
- Jensen, E. 2013, *Tapir: A Web Interface for Transit/Eclipse Observability*, Astrophysics Source Code Library, ascl:1306.007
- Kane, S. R., Ciardi, D. R., Gelino, D. M., & von Braun, K. 2012, *MNRAS*, **425**, 757
- Kass, R. E., & Raftery, A. E. 1995, *J Am Stat Assoc*, **90**, 773
- Kipping, D. M. 2013, *MNRAS*, **434**, L51
- Kirk, B., Conroy, K., Prša, A., et al. 2016, *AJ*, **151**, 68
- Kolbl, R., Marcy, G. W., Isaacson, H., & Howard, A. W. 2014, *AJ*, **149**, 18
- Königl, A., Giacalone, S., & Matsakos, T. 2017, *ApJL*, **846**, L13
- Kostov, V. B., Mullally, S. E., Quintana, E. V., et al. 2019, *AJ*, **157**, 124
- Kreidberg, L. 2015, *PASP*, **127**, 1161
- Lee, E. J., & Chiang, E. 2017, *ApJ*, **842**, 40
- Lightkurve Collaboration, Cardoso, J. V. d. M., Hedges, C., et al. 2018, *Lightkurve: Kepler and TESS time series analysis in Python*, Astrophysics Source Code Library, ascl:1812.013
- Lissauer, J. J., Marcy, G. W., Rowe, J. F., et al. 2012, *ApJ*, **750**, 112
- Lopez, E. D., & Fortney, J. J. 2013, *ApJ*, **776**, 2
- Mayo, A. W., Vanderburg, A., Latham, D. W., et al. 2018, *AJ*, **155**, 136
- McCauliff, S. D., Jenkins, J. M., Catanzarite, J., et al. 2015, *ApJ*, **806**, 6
- McKinney, W. 2011, *pandas: a Foundational Python Library for Data Analysis and Statistics*, <https://github.com/pandas-dev/pandas>
- Moe, M., & Di Stefano, R. 2017, *ApJS*, **230**, 15
- Morton, T. D. 2012, *ApJ*, **761**, 6
- Morton, T. D. 2015, *VESPA: False positive probabilities calculator*, Astrophysics Source Code Library, ascl:1503.011
- Morton, T. D., Bryson, S. T., Coughlin, J. L., et al. 2016, *ApJ*, **822**, 86
- Morton, T. D., & Swift, J. 2014, *ApJ*, **791**, 10
- Muirhead, P. S., Dressing, C. D., Mann, A. W., et al. 2018, *AJ*, **155**, 180
- Mulders, G. D., Pascucci, I., & Apai, D. 2015a, *ApJ*, **798**, 112
- Mulders, G. D., Pascucci, I., & Apai, D. 2015b, *ApJ*, **814**, 130
- Mulders, G. D., Pascucci, I., Apai, D., & Ciesla, F. J. 2018, *AJ*, **156**, 24
- Nutzman, P., & Charbonneau, D. 2008, *PASP*, **120**, 317
- Oliphant, T. E. 2006, *A Guide to NumPy*, Vol. 1 (Spanish Fork, UT: Trelgol Publishing)
- Petigura, E. A., Howard, A. W., & Marcy, G. W. 2013, *PNAS*, **110**, 19273
- Price-Whelan, A. M., Sipőcz, B., Günther, H., et al. 2018, *AJ*, **156**, 123
- Quinn, S. N., Becker, J. C., Rodriguez, J. E., et al. 2019, *AJ*, **158**, 177
- Ricker, G. R., Latham, D., Vanderspek, R., et al. 2010, *BAAS*, **42**, 459
- Sanchis-Ojeda, R., Rappaport, S., Winn, J. N., et al. 2014, *ApJ*, **787**, 47
- Santerne, A., Díaz, R., Almenara, J.-M., et al. 2015, *MNRAS*, **451**, 2337
- Santerne, A., Díaz, R., Moutou, C., et al. 2012, *A&A*, **545**, A76
- Shabram, M., Demory, B.-O., Cisewski, J., Ford, E. B., & Rogers, L. 2016, *ApJ*, **820**, 93
- Shallue, C. J., & Vanderburg, A. 2018, *AJ*, **155**, 94
- Sorahana, S., Yamamura, I., & Murakami, H. 2013, *ApJ*, **767**, 77
- Stassun, K. G., Oelkers, R. J., Pepper, J., et al. 2018, *AJ*, **156**, 102
- Swift, J. J., Johnson, J. A., Morton, T. D., et al. 2013, *ApJ*, **764**, 105
- Thompson, S. E., Coughlin, J. L., Hoffman, K., et al. 2018, *ApJS*, **235**, 38
- Torres, G., Andersen, J., & Giménez, A. 2010a, *A&ARv*, **18**, 67
- Torres, G., Fressin, F., Batalha, N. M., et al. 2010b, *ApJ*, **727**, 24
- Torres, G., Konacki, M., Sasselov, D. D., & Jha, S. 2004, *ApJ*, **614**, 979
- Torres, G., Konacki, M., Sasselov, D. D., & Jha, S. 2005, *ApJ*, **619**, 558
- Twicken, J. D., Catanzarite, J. H., Clarke, B. D., et al. 2018, *PASP*, **130**, 064502
- Vanderspek, R., Huang, C. X., Vanderburg, A., et al. 2019, *ApJL*, **871**, L24
- Virtanen, P., Gommers, R., Oliphant, T. E., et al. 2019, *NatMe*, **17**, 261